Mitochondrial-Localized Keratin 17 Promotes Chemoresistance in Basal-like Pancreatic Cancer

Chun-Hao Pan[1,2,3], Yinghuan Lyu[1,2], Monisankar Ghosh[1], Md Afjalus Siraj[4], Robert Tseng[1,4,5], Nina V. Chaika[6], John D. Haley[1], Bahman Khalvatifahlylani[1], David A. Tuveson[7], Hardik D. Patel[7], Muaz Faruque[4], Girish H. Rajacharya[8], Katie L. Donnelly[1], Cindy V. Leiton[1], Carlos Mauricio Mejia Arbelaez[4,9], Haoting Chen[4], Sumedha Chowdhury[4], Shayan Sarkar[1,2], Lyanne Delgado Coka[1,10], Lucia Roa-Peña[1,11], Michael Horowitz[1], Natalia Marchenko[1], Pankaj K. Singh[6,8], Kenneth R. Shroyer[1], and Luisa F. Escobar-Hoyos[1,4,12,13,14]

ABSTRACT

The basal-like molecular subtype of pancreatic ductal adenocarcinoma (PDAC) is highly lethal and therapy resistant. A better understanding of the underlying molecular mechanisms driving this aggressive tumor subtype is necessary for the development of effective therapies. Notably, upregulation of keratin 17 (K17) in cancer is associated with poor patient outcome and the basal-like PDAC subtype. In this study, we identified a critical dependency of basal-like PDACs on *de novo* pyrimidine biosynthesis, driven by intramitochondrial K17. Mechanistically, K17 translocated into the mitochondrial intermembrane space via a mitochondrial localization signal recognized by the translocase of outer mitochondrial membrane 20. In the mitochondria, K17 bound to and stabilized dihydroorotate dehydrogenase, the rate-limiting enzyme of *de novo* pyrimidine biosynthesis, by preventing its ubiquitination-mediated degradation. Blocking the entry of K17 into the mitochondria sensitized cancer cells to gemcitabine, a pyrimidine analogue and standard chemotherapeutic agent. In animal studies, pharmacologic inhibition of dihydroorotate dehydrogenase combined with gemcitabine treatment decreased tumor growth and doubled survival in mice bearing $K17^+$ but not $K17^-$ PDAC. These findings define a mitochondrial role for K17 in driving pyrimidine biosynthesis and uncover a metabolic vulnerability in $K17^+$ basal-like PDACs that can be therapeutically targeted.

Significance: Targeting the mitochondrial role of keratin 17 in pyrimidine biosynthesis represents a promising strategy to sensitize basal-like pancreatic cancer to gemcitabine and improve outcomes in this lethal subtype.

Introduction

Pancreatic ductal adenocarcinoma (PDAC) comprises two major molecular subtypes: "classical" (~60% of cases) and "basal-like" (~40% of cases), defined by distinct gene expression signatures that correlate with differences in survival and therapeutic response (1–3). Clinical evidence from the COMPASS trial (NCT02750657) demonstrates that these subtypes respond differentially to first-line chemotherapies; patients with basal-like tumors experience increased treatment-related adverse effects with m-FOLFIRINOX and derive greater benefit from gemcitabine/Abraxane, whereas patients with classical PDAC treated with m-FOLFIRINOX achieve the longest progression-free survival (4). Despite initial responses to first-line chemotherapy, basal-like PDACs frequently acquire resistance more rapidly (5, 6). Compounding this challenge, classical tumors can

[1]Department of Pathology, Renaissance School of Medicine, Stony Brook University, Stony Brook, New York. [2]Molecular and Cellular Biology Graduate Program, Stony Brook University, Stony Brook, New York. [3]Cancer Biology and Genetics Program, Sloan-Kettering Institute, Memorial Sloan Kettering Cancer Center, New York, New York. [4]Department of Therapeutic Radiology, Yale University, New Haven, Connecticut. [5]Department of Surgery, Yale University, New Haven, Connecticut. [6]Department of Pathology and Microbiology, University of Nebraska Medical Center, Omaha, Nebraska. [7]Cancer Center, Cold Spring Harbor Laboratory, Cold Spring Harbor, New York. [8]Department of Oncology Science, University of Oklahoma, Oklahoma City, Oklahoma. [9]Department of Pathology, Yale School of Medicine, New Haven, Connecticut. [10]Program of Public Health and Department of Preventive Medicine, Renaissance School of Medicine, Stony Brook University, Stony Brook, New York. [11]Department of Pathology, School of Medicine, Universidad Nacional de Colombia, Bogotá, Colombia. [12]Department of Molecular Biophysics and Biochemistry, Yale University, New Haven, Connecticut. [13]Department of Internal Medicine (Medical Oncology), Yale University School of Medicine, New Haven, Connecticut. [14]Yale Cancer Center, New Haven, Connecticut.

Current affiliations: Chun-Hao Pan, Cancer Biology and Genetics Program, Sloan-Kettering Institute, Memorial Sloan Kettering Cancer Center, New York, New York. Lucia Roa-Peña, Department of Pathology, School of Medicine, Universidad Nacional de Colombia, Bogotá, Colombia. Pankaj K. Singh, Department of Oncology Science, University of Oklahoma, Oklahoma City, Oklahoma.

C.-H. Pan, Y. Lyu, and M. Ghosh contributed equally to this article.

Corresponding Authors: Natalia Marchenko, Department of Pathology, Stony Brook University, 101 Nicolls Road, Stony Brook, NY 11794. E-mail: Natalia.Marchenko@stonybrookmedicine.edu; Kenneth R. Shroyer, Department of Pathology, Stony Brook University, 101 Nicolls Road, Stony Brook, NY 11794. E-mail: Kenneth.Shroyer@stonybrookmedicine.edu; Pankaj K. Singh, Department of Oncology Science, University of Oklahoma, 940 Stanton L. Young Blvd., Oklahoma City, OK 73104. E-mail: pankaj-singh@ouhsc.edu; Luisa F. Escobar-Hoyos, Department of Therapeutic Radiology, Yale University, 15 York Street, New Haven, CT 06513. E-mail: luisa.escobar-hoyos@yale.edu

Cancer Res 2026;86:2935–50

doi: 10.1158/0008-5472.CAN-25-4534

transition into the more aggressive basal-like subtype during treatment, further limiting durable therapeutic responses (7, 8). Together, these observations, supported by our retrospective analyses (9) and currently being evaluated in ongoing clinical trials (NCT06454383), underscore the urgent need to define the molecular mechanisms driving chemoresistance in basal-like PDAC to develop rational, subtype-specific therapeutic strategies.

Gemcitabine/Abraxane remains a standard-of-care regimen for PDAC and is frequently used as the control backbone for evaluating novel experimental therapies. Gemcitabine, a pyrimidine analogue, disrupts DNA replication and repair by preventing DNA elongation, thereby inducing cancer cell death (10). In response to the genotoxic effects of gemcitabine and other chemotherapeutic agents, cancer cells activate the *de novo* pyrimidine synthesis pathway to increase nucleotide availability required for DNA repair (11). Thus, blocking this pathway sensitizes cancer cells to DNA-damaging drugs (12, 13). Agents such as brequinar and the active metabolite of leflunomide, which target dihydroorotate dehydrogenase (DHODH), the rate-limiting mitochondrial enzyme in *de novo* pyrimidine synthesis, have been used to treat autoimmune disorders and prevent allograft rejection (14, 15). However, in a 1993 phase II clinical trial, brequinar monotherapy failed to yield objective responses in patients with pancreatic cancer (16). An ongoing clinical trial (NCT06454383) is evaluating leflunomide in combination with gemcitabine in patients with advanced unresectable pancreatic cancer. These clinical trials prompted us to investigate whether DHODH inhibition, when applied in the context of a biomarker-defined metabolic vulnerability, could enhance the therapeutic efficacy of pyrimidine analogues in PDAC.

Keratin 17 (K17) is normally expressed during embryogenesis, re-expressed as a hallmark of basal-like PDACs in both humans (17, 18) and mice (7, 8), and overexpressed in multiple other cancers (19–25). Based on these findings, we developed the "K17 test," an immunohistochemical assay designed to measure K17 levels in PDACs (17, 18, 26). This assay now serves as a companion diagnostic biomarker to identify basal-like tumors in ongoing clinical trials (NCT04469556 and NCT03991962) and was recently applied in a PDAC clinical study (27). Beyond its utility as a biomarker, K17 is a functional oncoprotein that promotes several hallmarks of cancer (28). It exerts its effects as both filamentous and soluble forms, located in the cytoskeleton, cytoplasm, and nucleus (21, 28, 29). Despite its established roles in tumor progression (21) and its correlation with chemoresistance to gemcitabine and 5-fluorouracil (5-FU; ref. 30), the precise functional role of K17 in mediating therapeutic resistance remains unknown.

Here, leveraging multiomics approaches, including *in silico* analysis of more than 400 PDAC cases, unbiased metabolomics, and animal studies, we identify a functional role of mitochondrial-localized K17 in promoting *de novo* pyrimidine synthesis and driving resistance to gemcitabine. Through functional mutagenesis, along with cellular and molecular studies, we found that K17 encodes a mitochondrial localization signal (MLS) and upon entry into mitochondria K17 binds to and stabilizes DHODH by preventing its degradation. In mouse models, we further showed that targeting DHODH in $K17^+$ PDACs, but not $K17^-$ PDACs, sensitizes tumors to gemcitabine and doubles mouse survival. Together, our findings reveal that K17 expression in basal-like tumors drives metabolic reprogramming and chemoresistance, offering a compelling rationale for selectively targeting DHODH in $K17^+$ PDAC to potentially enhance the effect of gemcitabine/Abraxane and improve patient survival.

Materials and Methods

Pathway and survival analyses from patient-derived data

Clinical annotations and transcripts per million RNA sequencing (RNA-seq) data of The Cancer Genome Atlas (TCGA) PAAD samples (31) were obtained from UCSC Xena Browser. Gene Ontology gene sets were downloaded from MSigDB collection. Single-sample gene set enrichment analysis (ssGSEA) was performed using the GSVA R package, which converts the gene-by-sample matrix into a pathway-by-sample matrix. Enrichment scores were determined using the ssGSEA method of Barbie and colleagues (32), which normalizes scores by the absolute difference between minimum and maximum. K17 mRNA levels were correlated with normalized enrichment scores (NES) using Spearman correlation, and NESs were compared between established high/low K17 groups (30) using the Wilcoxon rank-sum test. Top metabolic pathways were chosen based on the highest correlation and then significance.

Cell culture

The human L3.6 pancreatic adenosquamous cell line ($KRAS^{G12A}$; ref. 33) was provided by Dr. Wei-Xing Zong (Rutgers University). BxPC-3 (CRL-1687, $P53^{Y220C}$, RRID: CVCL_0186) and PANC-1 (CRL-1469, $KRAS^{G12D}$, $P53^{R273H}$, RRID: CVCL_0480) human PDAC cells were obtained and authenticated from the American Type Culture Collection (ATCC). A murine *Kras*$^{G12D/+}$; *p53*$^{R172H/+}$; *Pdx-Cre* (KPC) pancreatic cancer cell line was provided by Dr. Gerardo Mackenzie (University of California at San Diego). Cells were cultured at 37°C with 5% CO_2 in Dulbecco's Modified Eagle Medium (DMEM, Gibco, #11995073), supplemented with 10% fetal bovine serum (FBS, Corning, #35010CV) and 1% penicillin and streptomycin (Gibco, #15140122). Cells were routinely screened for *Mycoplasma* using a PCR-based detection kit (ATCC, #30-1012K) and were used at fewer than 10 passages from thawing. The culture conditions and genetic characterization of patient-derived organoids of PDAC have been described previously (34).

Genetic modification of K17 in pancreatic cancer cell lines

To generate K17 stable expression (SE) cell line models (L3.6, KPC, and PANC-1), cells were transduced with empty vector (EV), human K17 (K17), or K17 with mutated MLS (mMLS-K17) in medium containing 10% FBS for 24 hours, followed by fluorescence-activated cell sorting. Additionally, L3.6 and BxPC-3 K17 loss-of-function (LOF) models were created using CRISPR–Cas9–mediated knockout (KO), in which Cas9–single-guide RNA (sgRNA) ribonucleoproteins (sgRNA: CCAGTACTACAGGACAATTG) were electroporated using Synthego's protocol (Synthego).

Protein extraction and Western blot analysis

Cell lysates were prepared in RIPA buffer (Thermo Fisher Scientific, #87787) containing protease and phosphatase inhibitor cocktail (Thermo Fisher Scientific, #78440) and then sonicated and centrifuged to collect the supernatant. The protein concentration was measured using the Bradford assay (Bio-Rad, #5000202). Equal amounts of protein were resolved on 10% SDS-PAGE and transferred for immunoblotting with primary antibodies against K17 (provided by Dr. Pierre Coulombe, University of Michigan), α-tubulin (Abcam, #18251), DHODH (Cell Signaling Technology, #26381), pan-cadherin (Cell signaling Technology, #4073),

cytochrome c oxidase subunit IV (COX IV, Cell Signaling Technology, #4850), translocase of outer mitochondrial membrane (TOM) 20 (Proteintech, #11802-1-AP), TOM40 (Proteintech, #18409-1-AP), cytochrome c (Cell Signaling Technology, #11940), β-actin (Sigma-Aldrich, #A1978), Mitofilin (Santa Cruz Biotechnology, #sc-390707), and heat shock protein 60 (HSP60; Santa Cruz Biotechnology, #376261), followed by infrared goat anti–mouse or goat anti–rabbit IgG secondary antibodies (LI-COR Inc., #926-68071, #92632210). Blots were imaged on a LI-COR Odyssey system and quantified using Image Studio Lite (LI-COR Inc.).

Immunofluorescence and superresolution confocal imaging

Cells were fixed in ice-cold methanol (Thermo Fisher Scientific, #A412-4) at −20°C, permeabilized with 0.25% Triton X (Sigma-Aldrich, #X100), and blocked in PBS (Gibco, #14190250) containing 10% horse serum (Gibco, #26-050-070). Cells were incubated overnight with the primary K17 antibody, followed by a fluorophore-conjugated goat antirabbit secondary antibody (Invitrogen, #A-11008, #A-11005), counterstained with DAPI, and mounted with VECTASHIELD (Vector Laboratories, #H-1000-10, RRID: AB_2336789). For N-SIM (Nikon) superresolution imaging, cells on 0.2-mm coverslips were fixed in 4% paraformaldehyde in PBS for 15 minutes and then permeabilized, blocked, and stained using the same protocol, with secondary antibody incubation for 60 minutes at room temperature before mounting with Fluoromount-G (Thermo Fisher Scientific, #00-4958-02). Confocal images were acquired using a Zeiss LSM 980 Airyscan 2 NLO microscope and processed using Zeiss Zen 2 software. Quantification of TOM20 and K17 was performed by measuring the area of overlapping signal between K17 and TOM20 across 10 image areas.

Targeted metabolomics and ^{13}C-glucose–based flux analysis by mass spectrometry

Cells were plated in 6-cm dishes, and 2 hours before metabolite collection, the culture medium was replaced with fresh medium. Uniformly labeled ^{13}C-glucose was used for metabolic flux analysis. Polar and ^{13}C-labeled metabolites were extracted at the indicated time points and analyzed by LC/MS-MS using the selected reaction monitoring method with positive/negative ion switching on a Xevo TQ-S mass spectrometer (35, 36). Peak areas were integrated in MassLynx 4.1 (Waters Inc., RRID: SCR_014271), normalized to the respective protein concentrations, and subjected to relative quantification using MetaboAnalyst 3.0 (RRID: SCR_015539; ref. 37). Intracellular nucleoside fold changes were measured via mass spectrometry (MS) following exogenous nucleoside treatment for 1 hour. Relative quantification of gemcitabine and deoxycytidine (dC) in cell lysates was performed by calculating the ratio first and then normalizing it to the indicated controls.

Murine orthotopic xenograft studies

Cells were harvested and resuspended in a 1:1 mixture of DMEM with Matrigel (Life Sciences, #354234) at 1,000 cells in 30 μL. Cells were orthotopically implanted into the pancreas of 10-week-old mice. Tumor volume was monitored by ultrasound, and once tumor volume reached 50 mm^3, mice were randomized into treatment groups. Study I (gemcitabine chemoresistance): Female C57BL/6 albino (The Jackson Laboratory, RRID: IMSR_JAX:017840) mice were implanted with murine KPC EV and K17 cells and treated with (i) saline or (ii) gemcitabine (50 mg/kg) twice a week by intraperitoneal injection. Study II (gemcitabine and brequinar study): Immunodeficient NOD/SCID (The Jackson Laboratory, RRID: IMSR_JAX:001303) mice were implanted with human L3.6 K17 and K17 KO cells and treated with saline, gemcitabine (25 mg/kg) twice a week by intraperitoneal injection, and brequinar (10 mg/kg) twice a week by gavage, alone or in combination, for a total of 3 weeks. Gemcitabine and brequinar were dissolved in saline. Tumor growth and body weight were monitored weekly. All animal studies were approved by the institutional animal care and use committees of Stony Brook University and Yale University.

Compounds tested

Gemcitabine, brequinar, tetrahydrouridine, 6-mercaptopurine (purity>97%, Sigma-Aldrich, #G6423, #SML0113, #584222, and #852678), carbonyl cyanide 4-(trifluoromethoxy)phenylhydrazone (FCCP), and Gboxin (Selleck Chemicals, #S8276 and #S8828) were dissolved in 100% dimethyl sulfoxide (DMSO, Fisher Bioreagents, #BP231-100) with a stock concentration of 20 mmol/L and were prepared for cell experiments at final DMSO concentrations at 0.1%. Deoxyadenosine (dA), deoxyguanosine (dG), dC, and deoxythymidine (dT, purity > 99%, Sigma-Aldrich, #D8668, #T1895, #D3897, and #854999) were dissolved in water and administered at 100 μmol/L for nucleoside update, gemcitabine response, and cell proliferation experiments.

Cell viability and proliferation assays

Gemcitabine and deoxynucleoside supplements were optimized for each experiment. Cell viability was examined using CellTiter-Glo (CTG) luminescent cell viability assay (Promega, #G7570), WST-1 cell proliferation reagent (Sigma-Aldrich, #11644807001), CyQUANT reagent (Thermo Fisher Scientific, #C7026), or by crystal violet (Sigma-Aldrich, #32675) staining. Cells were plated and incubated overnight and drugs added with 10-point dose–response titrations in triplicate (0.5–20,000 nmol/L) or at the indicated concentration for 72 (CTG and CyQUANT) or 48 (WST-1) hours. The relative cell proliferation index and cell viability were measured by WST-1 or crystal violet staining assays at indicated time points. Briefly, 0.5% crystal violet in 20% methanol solution was used for staining, and 0.1 mol/L sodium citrate (Sigma-Aldrich, #W302600) in 25% ethanol solution (Pharmco, #111000200) was used for elution. Absorbance at 595 nm of eluted solution was measured.

RNA isolation and qRT-PCR

Total RNA was extracted with TRIzol reagent (Life Technologies, #10296010). cDNA synthesis was performed using MultiScribe Reverse Transcriptase (Thermo Fisher Scientific, #4311235), with 1 μg of RNA as a template for cDNA generation. TaqMan Universal Master Mix II, no UNG (Applied Biosystems, #4440043) was used, and qRT-PCR was programmed using a QuantStudio 3 real-time PCR system (Thermo Fisher Scientific).

RNA-seq analysis

RNA-seq library preparation was done using the Illumina TruSeq RNA library preparation kit. Sequence information was extracted with bcl2fastq 1.8.4; raw reads were aligned to GENCODE annotation GRCh38 v28 (*Homo sapiens*) or GRCm39 vM18 (*Mus musculus*) using STAR v2.7.3a, and raw gene counts were obtained and normalized with kallisto 0.46.2. Differential gene expression was then quantified using DESeq2 v1.10.1.

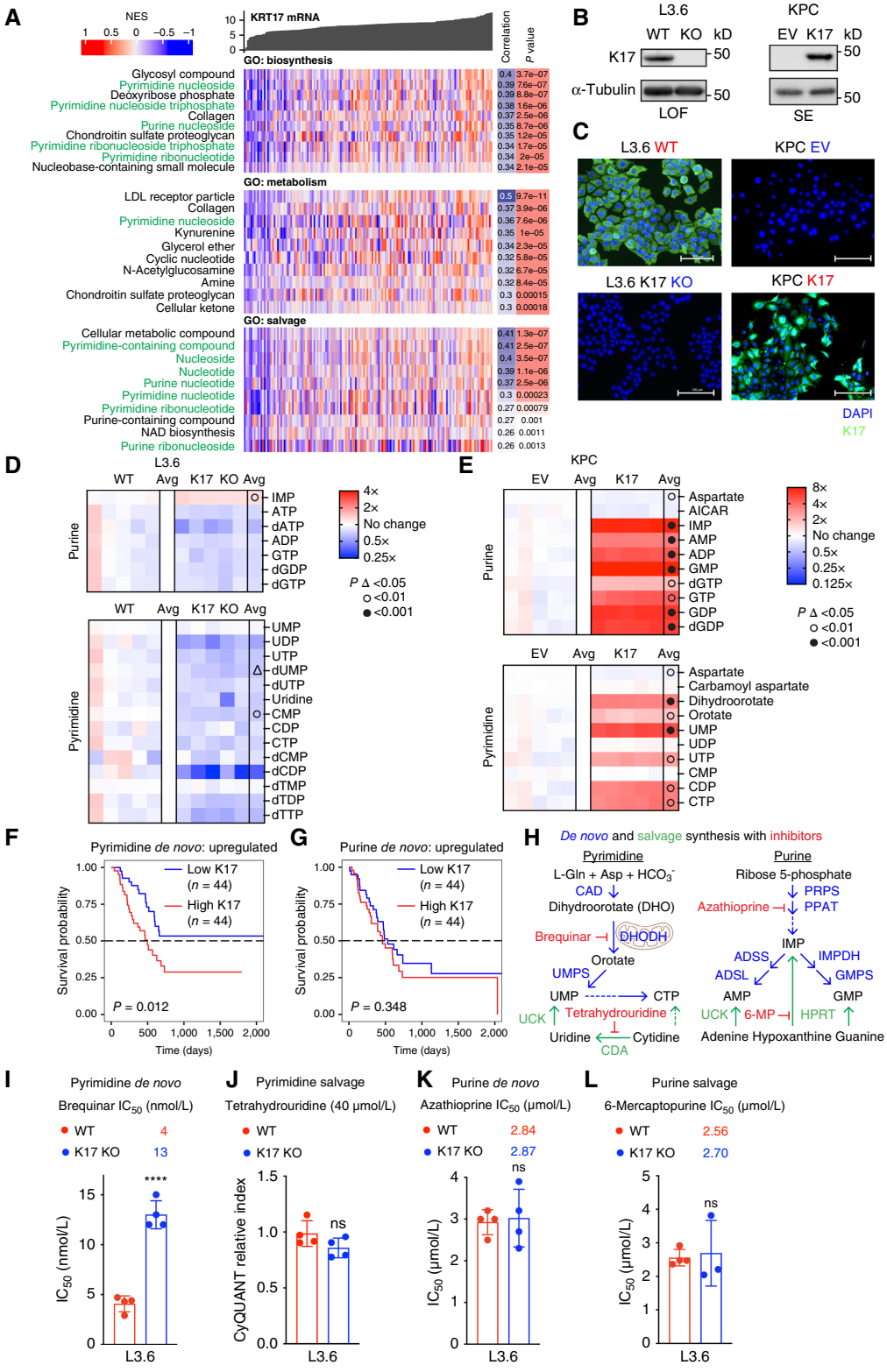

Figure 1.

K17-expressing pancreatic cancer cells rely on *de novo* pyrimidine biosynthesis. **A,** ssGSEA of K17 and Gene Ontology (GO) gene sets using TCGA data. K17 mRNA levels are correlated with NES using the Spearman correlation. *P* values are provided. **B,** Genetic manipulation of K17 expression to generate stable cell line models. CRISPR-mediated KO of K17 and a negative control (WT) are performed in the L3.6 human pancreatic (*Continued on the following page.*)

Generation of DHODH knockdown and CRISPR–Cas9–mediated KO cells

Transfection with small interfering RNAs (siRNA) was performed using the DharmaFECT system (Horizon Discovery). Four constructs of siRNA—ON-TARGETplus siRNA J-009619-05 (UAAAUUCCGAAAUCCAGUA), J-009619-06 (CCACGGGAGAUGAGCGUUU), J-009619-07 (GGACGGACUUUAUAAGAUG), and J-009619-08 (GAACACAGGUUACGGGCCA)—and nontargeting siRNA (UGGUUUACAUGUCGACUAA) were used. Briefly, L3.6 cells were grown to 50% confluence in antibiotic-free 10% DMEM and then transfected with the plasmids for 24 hours. For the drug treatment experiment, cells were replaced with 10% DMEM with indicated drugs 24 hours after transfection. To generate the KPC DHODH KO cell line model, an Edit-R–predesigned all-in-one lentiviral sgRNA (target sequence: ATAAATTCCGAAATCCAGTA) and nontargeting control (Horizon Discovery) were used. Briefly, cells were grown to 80% confluence and then transfected with the virus, followed by fluorescence-based cell sorting. Knockdown and KO efficiency was determined by Western blot analysis.

K17 mitochondria localization signal prediction

The prediction scores of K17 potential mitochondria localization sequences were explored using MitoProt II V1.101, based on the canonical N-terminal amphiphilic helix structure of MLS. TUBA1A (cytosolic), COX IV, and asparaginyl-tRNA synthetase 2 (NARS2; mitochondrial) were included as controls. K17 with mutated MLS (mMLS-K17) was generated by substituting positively charged amino acids at the N-terminus with alanine.

Mitochondria isolation assay and proteinase K digestion

Cells were harvested and washed with cold PBS. Mitochondrial and cytosol fractions were prepared with the Mitochondrial Isolation Kit for Cultured Cells (Thermo Fisher Scientific, #89874). Mitochondrial pellets were lysed either using RIPA buffer (Thermo Fisher Scientific, #87787) for protein quantification or in Pierce IP lysis buffer (Thermo Fisher Scientific, #87787) for immunoprecipitation assay. In the proteinase K limited digestion assay, mitochondrial pellets were resuspended in 1× TD buffer [50 mmol/L Trizma base, 274 mmol/L NaCl, 20 mmol/L KCl, and 14 mmol/L Na_2HPO_4; ref 38] and equally divided into four samples. Proteinase K solution (10 μg of proteinase K/mg of mitochondrial protein, Thermo Fisher Scientific, #EO0491) was added in the first sample, Triton X (2 mg of Triton X/mg of mitochondrial protein) was added in the second sample, both proteinase K and Triton X were added in the third sample, and the fourth sample was used as a no-treatment control. All four samples were kept at room temperature for 10 minutes while mixing every 3 minutes. A measure of 1 μL of 100 mmol/L phenylmethylsulfonyl fluoride (PMSF; Sigma-Aldrich, #78830, RRID: SCR_000488) was added into the four samples and mixed to stop digestion. The samples were processed for Western blot analysis.

Sodium carbonate extraction

Sodium carbonate extraction was performed as described in (39). Mitochondrial pellets were resuspended in buffer C (320 mmol/L sucrose, 1 mmol/L ethylenediaminetetraacetic acid (EDTA), and 10 mmol/L Tris-Cl pH 7.4), buffer C containing 1% Triton X, or 0.1 mol/L Na_2CO_3 (pH 11). Samples were incubated at 4°C for 1 hour with gentle nutation and then centrifuged to separate supernatant and pellet. Equal amounts from each fraction were analyzed by SDS-PAGE and immunoblotting.

Mitochondrial membrane fractionation

Mitochondria were isolated using isotonic buffer (250 mmol/L sucrose, 1 mmol/L EDTA, 10 mmol/L HEPES-KOH) pH 7.4, protease inhibitors, and 1 mmol/L PMSF). Pellets were resuspended to obtain 1 mg/mL protein and treated with increasing concentrations of digitonin (0%–0.25%) for 1 hour at 4°C. Soluble and insoluble fractions were separated by centrifugation at 20,000 × *g* (4°C), and insoluble pellets were resuspended in isotonic buffer to match the supernatant volume. Fractions were lysed and analyzed by SDS-PAGE and immunoblotting.

Immunoprecipitation and ubiquitination assay

For co-immunoprecipitation and to measure the ubiquitination of proteins, cells were washed with PBS and mitochondria were harvested as noted above. Before immunoblotting, lysate was clarified by centrifugation at 13,000 × *g* (4°C) for 15 minutes and then immunoprecipitated with K17 antibody (KDx, E-3, mouse monoclonal antibody targeting human K17), conjugated to magnetic beads (Invitrogen, #14311D) overnight. For the ubiquitination assay, cell lysates were immunoprecipitated with DHODH antibody (Proteintech, #14877-1-AP) conjugated to magnetic beads and analyzed by Western blot analysis using a horseradish peroxidase–conjugated antiubiquitin antibody (A-5, Santa Cruz Biotechnology, #sc-166553).

Statistics

Drug pair interactions were calculated using the highest single agent model on Combenefit software (Cancer Research UK Cambridge Institute, version 2.021; ref. 40). Statistical analyses, including calculation of half-maximal inhibitory concentrations (IC_{50}) and survival, were performed using GraphPad Prism 7 (RRID: SCR_002798). Two-group comparisons were conducted using the Welch *t* test, one-way ANOVA was used for comparisons among more than two groups, and two-way ANOVA was

(*Continued.*) cancer cell line to generate a K17 LOF model. Murine *Kras*$^{G12C/+}$; *Trp53*$^{R172H/+}$; *Pdx-Cre* (KPC) pancreatic cancer cells are transduced to stably express either EV or human K17 as SE models. **C,** Immunofluorescence images of K17 LOF and SE cell line models. Green, filamentous form of K17; blue, nucleus indicated by DAPI stain. Scale bars, 100 μm. **D** and **E,** Metabolomics analyses in K17 LOF (**D**) and SE (**E**) cell line models. Data are shown in heatmaps with $n = 5$ per group. Two-way ANOVA followed by the Šídák test. Statistical significance between groups is indicated. AICAR, 5-aminoimidazole-4-carboxamide ribonucleotide. **F** and **G,** Kaplan–Meier survival curves stratifying patients based on K17 mRNA expression and gene set enrichment scores for nucleotide biosynthesis pathways. $n = 44$ cases per group. Log-rank *P* values are shown. **H,** Outline of the nucleotide biosynthesis pathway and compounds that target *de novo* or salvage synthesis of purine and pyrimidine. CDA, cytidine deaminase; PPAT, phosphoribosyl pyrophosphate amidotransferase; UMPS, uridine monophosphate synthetase; UCK, uridine–cytidine kinase; PRPS, phosphoribosyl pyrophosphate synthetase; ADSS, adenylosuccinate synthase; ADSL, adenylosuccinate lyase; IMPDH, inosine monophosphate dehydrogenase; GMPS, guanosine monophosphate synthetase. **I–L,** Drug sensitivity of L3.6 K17 LOF cells to inhibitors of nucleotide metabolism, including brequinar (*de novo* pyrimidine, **I**), tetrahydrouridine (pyrimidine salvage, **J**), azathioprine (*de novo* purine, **K**), and 6-mercaptopurine (6-MP; purine salvage, **L**), shown as IC_{50} values or relative viability. Mean ± SD; $n = 4$; Welch *t* test. ns, not significant, ****, $P < 0.0001$. **H,** created in BioRender. Pinto medici, N. (2026) https://BioRender.com/k6ed1uz.

applied for analyses involving multiple variables. Kaplan–Meier survival analysis was performed using two-group comparisons, reporting log-rank hazard ratios and P values. Data were expressed as means ± standard deviation (SD), and *, $P < 0.05$; **, $P < 0.01$; ***, $P < 0.001$; ****, $P < 0.0001$ were considered significant.

Results

K17$^+$ pancreatic cancer cells depend on *de novo* pyrimidine biosynthesis

Prompted by clinical observations that the expression of K17 in PDACs correlates with gemcitabine resistance (30), we set out to determine the relationship between K17 and metabolic profiles. Using unsupervised clustering based on K17 mRNA levels and GSEA in untreated primary PDACs from TCGA, we found that K17 expression was significantly correlated with pathways related to pyrimidine and purine metabolism, with enrichment scores ranging from 0.26 to 0.41 (**Fig. 1A**). For comparison, the highest enrichment score in an unbiased analysis was 0.56 (Supplementary Fig. S1A). As these correlations were derived from cohort-normalized data without accounting for patient-specific variables, we generated well-controlled isogenic cell line models to test whether K17 directly promotes nucleotide biosynthesis.

We performed unbiased metabolomics profiling studies in isogenic K17$^+$ versus K17$^-$ PDAC cell lines from humans and mice using both LOF and SE approaches (**Fig. 1B** and **C**; Supplementary Fig. S1B and S1C). Briefly, we generated a K17 KO in the human L3.6 cell line, which expresses wild-type (WT) K17 as an LOF model and stably expressed EV or human K17 in murine *Kras*$^{G12D/+}$; *Trp53*$^{R172H/+}$; *Pdx-Cre* (KPC) and human PANC-1 cell lines as SE models. K17 expression promoted a twofold increase in intracellular purines and pyrimidines compared with control cells (**Fig. 1D** and **E**; Supplementary Fig. S1D–S1G). Metabolites upstream of nucleotide metabolism, including glycolysis, the tricarboxylic acid cycle, and the pentose phosphate pathway (PPP), were also modestly upregulated in K17$^+$ cells but to a lesser extent than nucleotide metabolites (Supplementary Fig. S2A–S2D). These results suggest that K17 functionally drives metabolic reprogramming to enhance nucleotide production.

To evaluate differential nucleotide dependencies in K17$^+$ PDACs, we evaluated the transcriptional signatures of purine and pyrimidine biosynthetic pathways and patient survival in cases with low versus high K17 expression. Upregulation of *de novo* biosynthesis of pyrimidines was associated with shorter survival in patients with high K17-expressing PDACs compared with low K17 expression (log-rank $P = 0.012$, **Fig. 1F**). In contrast, *de novo* purine biosynthesis showed no significant association with survival based on K17 expression (log-rank $P = 0.348$, **Fig. 1G**). Similarly, K17 status did not associate with patient survival relative to salvage pathways for pyrimidines (log-rank $P = 0.062$) or purines (log-rank $P = 0.778$; Supplementary Fig. S3A and S3B). Consistently, patients with overall upregulated nucleotide metabolism in their tumors exhibited shorter survival than those with downregulated nucleotide metabolism (Supplementary Fig. S3C). These data led us to hypothesize that K17-expressing cells rely on the *de novo* pyrimidine biosynthetic pathway.

To test this, we assessed the dependency of K17$^+$ PDAC cells on specific nucleotide pathways by treating K17$^+$ and K17$^-$ cells with FDA-approved inhibitors that target various nucleotide biosynthetic routes (**Fig. 1H** and Supplementary Table S1; refs. 41, 42). Based on literature review, we identified 27 candidate molecules and excluded those that did not show specificity for K17$^+$ cells based on our published high-throughput drug screen assays (Supplementary Table S1; ref. 30). We then selected four compounds for targeted testing (**Fig. 1H**). L3.6 K17 WT cells were three times more sensitive to brequinar, an inhibitor of *de novo* pyrimidine biosynthesis, than K17 KO cells (**Fig. 1I**). In contrast, there were no significant differences in cytotoxicity between K17 WT and K17 KO cells when treated with inhibitors of the pyrimidine salvage pathway (tetrahydrouridine), the purine *de novo* biosynthesis (azathioprine), or the purine salvage pathway (6-mercaptopurine; **Fig. 1J–L**). Similar results were observed in the murine KPC isogenic PDAC cells (Supplementary Fig. S3D–S3H). Together, these findings suggest that K17$^+$ PDAC cells are specifically dependent on pyrimidine *de novo* biosynthesis for survival.

Increased dC in K17$^+$ pancreatic cancer cells drives resistance to gemcitabine

The dependency of K17$^+$ PDAC cells on *de novo* pyrimidine biosynthesis led us to hypothesize that K17 drives resistance to gemcitabine, a dC analogue, via molecular competition between dC and gemcitabine. We previously showed that orthotopically transplanted KPC K17-expressing PDACs did not respond to gemcitabine (30). To further demonstrate that K17 drives resistance to gemcitabine, we treated mice bearing orthotopic syngeneic murine KPC EV or K17 PDACs with gemcitabine. Gemcitabine significantly extended survival in mice bearing EV tumors (log-rank $P = 0.0001$, **Fig. 2A**) but not in mice with K17$^+$ tumors (log-rank $P = 0.08$, **Fig. 2B**), consistent with our prior patient data (9), preclinical studies (30), and clinical trial observations (4).

We next hypothesized that increased intracellular dC contributes to gemcitabine resistance. In rescue experiments, we supplemented K17$^-$ and K17$^+$ PDAC cells with individual nucleosides (dA, dG, dC, and dT) in the presence of gemcitabine. Upon exogenous nucleoside treatment, MS first confirmed the expected increases in intracellular dA, dG, and dC, whereas dT uptake was less pronounced (Supplementary Fig. S3I). Under gemcitabine treatment, dC conferred the strongest rescue effect (at least five times higher), promoting resistance in L3.6 K17 KO cells to levels comparable with K17 WT cells only treated with gemcitabine (**Fig. 2C**; Supplementary Figs. S3J and S4A). Similar results were observed in murine KPC isogenic models (**Fig. 2D**; Supplementary Figs. S3K and S4B). Of note, K17$^+$ PDAC cells were four times more resistant to gemcitabine in the presence of dCs, compared with K17$^-$ cells (**Fig. 2E** and **F**; Supplementary Figs. S3L and S3M and S4C and S4D), suggesting that independent of *de novo* pyrimidine biosynthesis, exogenous dC promotes gemcitabine resistance regardless of K17 status. This resistance phenotype was not driven by altered cell proliferation, as supplementing individual nucleosides did not affect growth rates between K17$^+$ and K17$^-$ cells (Supplementary Fig. S4E–S4H). Lastly, we did not observe significant differences in cell growth (Supplementary Fig. S4I–S4K) or cell-cycle progression (Supplementary Fig. S4L–S4N) between cells with or without K17, ruling out the possibility that increased pools of nucleotide reflected rapid cell proliferation.

To determine whether dC-mediated resistance to gemcitabine arises from intracellular molecular competition, we measured intracellular dC and gemcitabine levels using LC/MS-MS. Compared with K17$^-$ cells, K17$^+$ cells maintained a higher dC:gemcitabine ratio (**Fig. 2G** and **H**; Supplementary Fig. S4O), suggesting that elevated endogenous dC competes with gemcitabine, thereby

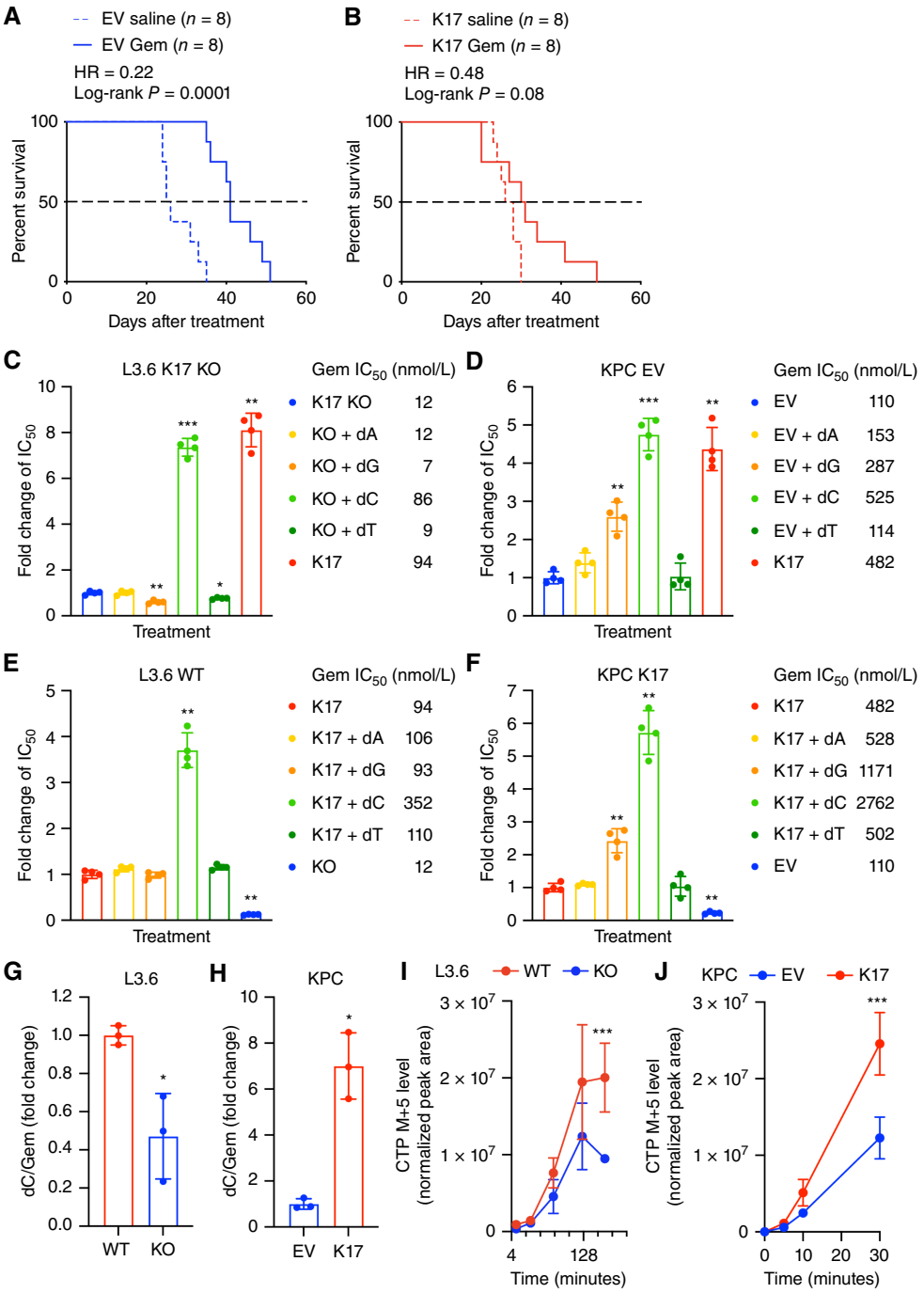

Figure 2.

Elevated dC levels promote gemcitabine resistance in K17$^+$ pancreatic cancer cells. **A** and **B,** Kaplan–Meier survival curves of mice bearing K17$^-$ and K17$^+$ tumors treated with gemcitabine (Gem) or saline control. $n = 8$ per arm. Log-rank hazard ratio (HR) and P values are shown. **C** and **D,** Exogenous treatment of dA, dG, dC, or dT combined with gemcitabine in K17$^-$ cell lines. The IC_{50} values are shown. **E** and **F,** Exogenous treatment of dA, dG, dC, or dT combined with gemcitabine in K17$^+$ cell lines. The IC_{50} values are shown. Mean ± SD; $n = 4$; Brown–Forsythe and Welch ANOVA followed by the Dunnett T3 test. **G** and **H,** Deoxycytidine/gemcitabine ratio upon gemcitabine treatment, as determined by LC/MS-MS in K17 LOF (**G**) and SE (**H**) cell line models. Mean ± SD; $n = 3$; Welch test. **I** and **J,** ^{13}C-Glucose metabolic flux analysis in K17 LOF (**I**) and SE (**J**) cell line models to measure CTP flux. Mean ± SD; $n = 3$; two-way ANOVA followed by the Tukey test. *, $P < 0.05$; **, $P < 0.01$; ***, $P < 0.001$.

reducing gemcitabine efficacy. Next, we evaluated the dynamics of autonomous *de novo* pyrimidine production by measuring intracellular cytidine triphosphate (CTP) levels over time. Using ^{13}C labeling flux analyses, we observed that K17$^+$ cells incorporated ^{13}C into CTP more rapidly and to a greater extent than K17$^-$ cells (**Fig. 2I** and **J**), indicating enhanced *de novo* cytosine biosynthesis. Interestingly, K17$^+$ L3.6 cells showed a transient increase in glucose relative to K17$^-$ cells, followed by a decline, consistent with rapid flux through glucose 6-phosphate (G6P) toward lactate, whereas KPC EV cells showed higher glucose levels than KPC K17 cells without changes in the G6P or lactate level (Supplementary Fig. S4P). These findings indicate that K17-driven glycolytic reprogramming, as measured by dynamic flux tracing, is context dependent and model specific. Together, this K17-driven increase in cytosines boosts the nucleotide pool required for DNA/RNA synthesis and repair, supporting the mechanism by which K17 drives gemcitabine chemoresistance through molecular competition with dC.

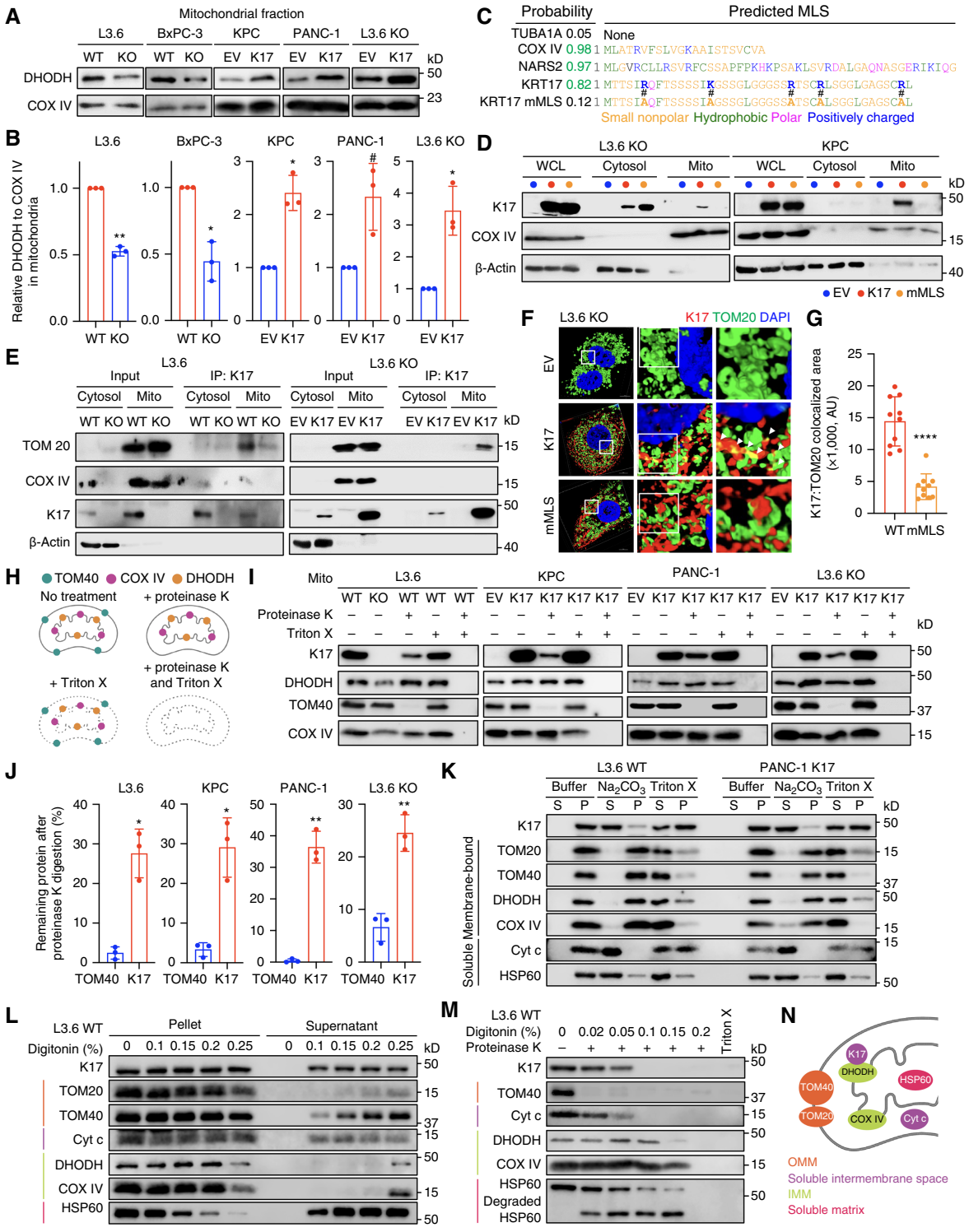

Figure 3.

K17 localizes to the mitochondria via a functional MLS and increases mitochondrial DHODH levels. **A,** Western blots of mitochondrial subcellular fractions of DHODH and COX IV in K17 LOF, SE, and rescue cell line models. **B,** Representative bar graphs show the fold change in mitochondrial DHODH levels normalized to the mitochondrial protein COX IV. Mean ± SD; $n = 3$; Welch t test. #, $P = 0.0669$. **C,** Predicted mitochondrial localization signal (MLS) in K17, identified by MitoProt II based on a canonical N-terminal amphipathic helix. TUBA1A (cytosolic), COX IV, and NARS2 (mitochondrial) were included as controls. An MLS LOF mutant of K17 (mMLS-K17) was generated by substituting positively charged amino acids with alanine. The MLS probability scores are shown. **D,** Western blots of whole-cell lysate (WCL) and cytosolic and mitochondrial (Mito) subcellular fractions of K17, COX IV, and β-actin in human (*Continued on the following page.*)

As the uptake of nucleosides may also affect the efficacy and resistance of gemcitabine, we evaluated the expression of major nucleoside transporters. We found that the mRNA and protein levels of key nucleoside transporters were similar in $K17^+$ and $K17^-$ cells (Supplementary Fig. S4Q–S4S). Moreover, no significant difference was observed in genes involved in PPP and the pyrimidine biosynthesis pathway, as determined by RNA-seq analysis in isogenic pairs (Supplementary Fig. S5). Overall, these results indicate that gemcitabine resistance in $K17^+$ cells is driven by intracellular dC levels through a cell-autonomous and posttranscriptional mechanism.

K17 translocates to and localizes within the mitochondrial intermembrane space

We next investigated the mechanism by which K17 increases intracellular pyrimidine levels. We focused on DHODH, a mitochondrial-localized enzyme that connects two major intracellular processes: *de novo* pyrimidine biosynthesis (43) and electron transfer from dihydroorotate to ubiquinone as part of the mitochondrial electron transport chain (44). In addition, DHODH is the target of brequinar, the pyrimidine *de novo* biosynthesis inhibitor that selectively kills $K17^+$ cells (**Fig. 1I**). For *de novo* pyrimidine biosynthesis, DHODH promotes the oxidation of dihydroorotate to orotate, a key step in the synthesis of uridine monophosphate, the precursor for other pyrimidines such as cytidine (45). Although DHODH mRNA levels were comparable between $K17^+$ and $K17^-$ cells (Supplementary Fig. S5C and S5D), we observed a two- to fourfold increase in DHODH protein levels in the mitochondria fraction of $K17^+$ cells (**Fig. 3A** and **B**; Supplementary Fig. S6A–S6E), using K17 LOF (L3.6 and BxPC-3), SE (KPC and PANC-1), and rescue (re-expressing either empty vector [EV] or K17 in L3.6 K17 knockout cells) cell line models. These findings suggest that K17 affects DHODH through posttranscriptional regulation or enhanced mitochondrial localization. Remarkably, K17 was detected in these same mitochondrial fractions, unveiling a previously unrecognized mitochondrial localization of this cytoskeleton protein (Supplementary Fig. S6A– S6E).

To dissect the mechanism through which K17 localizes in the mitochondria, we assessed whether K17 contains a mitochondrial localization signal (MLS). The MLS is typically located at the N-terminus of precursor proteins and forms an amphipathic α-helix, characterized by positively charged residues on the one side and hydrophobic residues on the other side (46). This structure is crucial for recognition by the mitochondrial import machinery, including the TOM complex, to guide the protein to the mitochondria (47–49). Using the MitoProt sequence prediction platform (50), we identified that the first 42 residues at the N-terminus of K17 constitute a potential MLS, with a probability score of 82%, similar to other established MLSs from other mitochondrial-localized proteins such as COX IV (98%) and NARS2 (97%; **Fig. 3C**). To functionally validate the predicted MLS of K17, we generated an MLS LOF mutant (mMLS) by substituting five positively charged amino acids of the MLS with alanine (R6A, K15A, R26A, R30A, and R41A). This mMLS-K17 decreased the MitoProt probability of a functional MLS to 12%. In line with our prediction, mutations in the MLS abolished the mitochondria localization of K17, and mMLS-K17 was restricted to the cytosolic fraction in cells, in contrast to cells expressing WT K17 (**Fig. 3D**). To further elucidate how K17 enters the mitochondria, we performed immunoprecipitation of K17 from the mitochondrial fraction to assess its interaction with the mitochondrion-importing complex TOM. Immunoprecipitation assays revealed that K17 interacts with TOM20, the receptor in the TOM complex that recognizes the MLS in proteins (**Fig. 3E**; Supplementary Fig. S6F–S6H; refs. 48, 51). These interactions were further validated using immunofluorescence staining and confocal microscopy. Supporting our hypothesis, cells with mMLS had significantly lower colocalization of K17 and TOM20 (**Fig. 3F** and **G**; Supplementary Fig. S6I and S6J), and the average Pearson correlation coefficient between K17 and TOM20 was significantly higher in L3.6 WT cells (0.143 ± 0.072, mean ± SD) than in L3.6 K17-mMLS cells (0.058 ± 0.045, mean ± SD; $n = 10$ images; Welch t test, $P = 0.0065$). Of note, no significant differences in cell proliferation were observed among cells expressing EV, K17, or mMLS-K17 (Supplementary Fig. S6K).

To define the precise localization of K17 within mitochondria, we performed submitochondrial fractionation (38) followed by proteinase K treatment (52), which digests proteins that are embedded in the outer membrane, such as TOM40 (**Fig. 3H**). Our data showed that treatment with proteinase K, which digests the outer mitochondrial membrane proteins, including TOM40 (**Fig. 3I**), did not eliminate K17 (**Fig. 3J**). To confirm the efficacy of proteinase K in digesting K17, Triton X was included as a membrane permeabilizer control. The persistence of K17 after digestion suggests that a fraction of K17 enters mitochondria (**Fig. 3I**; Supplementary Fig. S6L). These results also helped rule out the possibility that the previously observed mitochondrial localization of K17 was due to minor cytosolic contamination in the isolated mitochondrial fractions. To determine whether K17 is membrane-bound within mitochondria, we performed transmembrane domain (TMD) prediction and sodium carbonate extraction. No TMD was predicted using DeepTMHMM (bioRxiv 2022.04.08.487609), and K17 was not detected in the pellet fraction of the sodium carbonate lysate (**Fig. 3K**), suggesting that K17 is not a mitochondrial membrane-bound protein. Consistent with this, K17 was rapidly released into the supernatant independent of digitonin concentration, suggesting

(*Continued.*) L3.6 and murine KPC cell line models. Note: The COX IV and β-actin loading controls were intentionally reused in **Fig. 4A**. **E,** Western blots show immunoprecipitation (IP) of K17 with TOM20 and COX IV in cytosolic and mitochondrial fractions from K17 LOF and rescue cell line models. An input control of cell lysates is included. Note: COX IV, K17, and β-actin were intentionally reused in **Fig. 4C**. **F** and **G,** Immunofluorescent images of K17 (red), TOM20 (green), and nucleus (blue) in L3.6 K17 rescue cell line models captured by superresolution confocal microscopy. Bar graph indicates the colocalized area of K17 and TOM20. Mean ± SD; $n = 10$ images; Welch t test. **H,** Outline of the experimental design of the limited digestion assay to determine the submitochondrial localization of K17. Proteinase K selectively digests outer membrane proteins, whereas Triton X permeabilizes both the outer and inner mitochondrial membranes. **I** and **J,** Western blots of mitochondrial fractions showing K17, DHODH, TOM40, and COX IV following the limited digestion assay in K17 LOF, SE, and rescue cell line models (**I**). Bar graphs show the percentage of each indicated protein remaining after proteinase K treatment (**J**). Mean ± SD; $n = 3$; Welch t test. **K,** Mitochondrial proteins from L3.6 WT cells were extracted using buffer alone, Na_2CO_3 solution, or buffer containing 1% Triton X. S, supernatant; P, pellet. **L,** Extraction of mitochondrial proteins from L3.6 WT cells using increasing concentrations of digitonin. **M,** Proteinase K protection assay under digitonin performed on mitochondria isolated from L3.6 WT cells. **N,** TOM20 and TOM40 are outer mitochondrial membrane (OMM) proteins; K17 and cytochrome c (Cyt c) reside in the mitochondrial intermembrane space; DHODH and COX IV are inner mitochondrial membrane (IMM) proteins; and HSP60 is localized to the mitochondrial matrix. *, $P < 0.05$; **, $P < 0.01$; ****, $P < 0.0001$. **H** and **N,** created in BioRender. Pinto medici, N. (2026) https://BioRender.com/k6ed1uz.

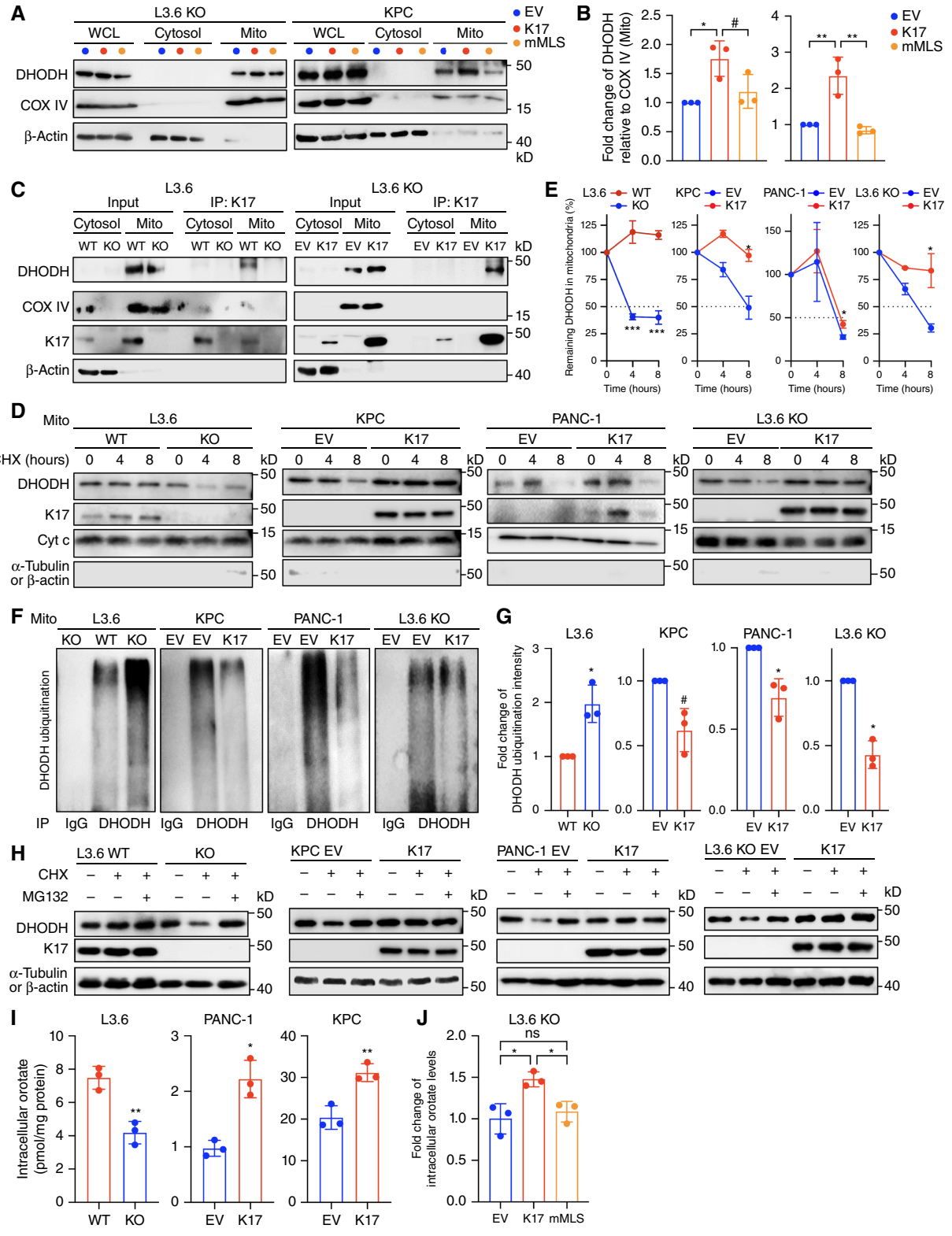

Figure 4.

K17 stabilizes mitochondrial DHODH to promote *de novo* pyrimidine biosynthesis. **A,** Western blots of whole-cell lysate (WCL) and cytosolic and mitochondrial (Mito) subcellular fractions of DHODH, COX IV, and β-actin in human L3.6 and murine KPC cell line models. Note: The COX IV and β-actin loading controls were intentionally reused in **Fig. 3D**. **B,** Fold change of mitochondrial DHODH relative to COX IV. Mean ± SD; $n = 3$; one-way (*Continued on the following page.*)

greater solubility of K17 relative to membrane-bound proteins (**Fig. 3L**). With increasing digitonin concentrations, proteinase K progressively digested accessible proteins, whereas Triton X served as a positive control. Under these conditions, the K17 digestion pattern was intermediate between outer and inner mitochondrial membrane proteins and closely resembled that of cytochrome c (**Fig. 3M**). Together, these data suggest that K17 contains an MLS that enables its entry into the mitochondrial intermembranous space (**Fig. 3N**).

K17 binds to and stabilizes DHODH in the mitochondria, thereby promoting *de novo* pyrimidine biosynthesis

Given that K17 expression increases the levels of DHODH in the mitochondria (**Fig. 3A**), we set out to elucidate the underlying mechanism. First, we found that DHODH was significantly reduced in mMLS-K17 cells compared with WT K17$^+$ cells, suggesting that mitochondrial entry of K17 is required to maintain DHODH levels (**Fig. 4A** and **B**). Second, as both K17 and DHODH localize to the mitochondria (**Fig. 3J** and **K**), we performed immunoprecipitation using mitochondrial and cytosolic fractions and found that K17 specifically interacts with DHODH within the mitochondria (**Fig. 4C**; Supplementary Fig. S6F–S6H). We also observed this K17–DHODH interaction in patient-derived organoids of PDAC (Supplementary Fig. S6M). As DHODH resides in the mitochondrial inner membrane facing the intermembrane space (53) and K17 is soluble within this space, their interaction most likely occurs there (**Fig. 3N**). Of note, K17 did not interact with COX IV, another inner membrane–associated protein, indicating that the interaction of K17 and DHODH is selective (**Fig. 4C**).

DHODH is the rate-limiting enzyme for *de novo* pyrimidine biosynthesis, and previous studies have shown that its stability can be regulated by protein–protein interactions (54). Given the interaction of K17 with DHODH, we next examined the half-life of DHODH in the mitochondria in the presence or absence of K17. Following treatment with cycloheximide (CHX), we found that the half-life of DHODH was approximately 8 hours in K17$^-$ cells. In contrast, nearly all DHODH was retained at the same time point in K17$^+$ cells (**Fig. 4D** and **E**; Supplementary Fig. S7A–S7D), indicating that K17 significantly enhances DHODH stability. Mitochondrial proteins are ubiquitinated within the mitochondria (matrix, inner membrane, and intermembrane space) and exported to the cytosol for proteasomal degradation (55–57). As previous reports indicate that DHODH is subject to ubiquitin-mediated degradation (54), we next determined if K17 stabilizes DHODH by inhibiting its ubiquitination and subsequent degradation. We found that mitochondrial DHODH was approximately twofold more ubiquitinated in K17$^-$ compared with K17$^+$ cells (**Fig. 4F** and **G**; Supplementary Fig. S8A–S8J). We also demonstrated that treatment with the proteasome inhibitor MG132 significantly rescued DHODH levels in K17$^-$ cells compared with K17$^+$ cells under CHX treatment (**Fig. 4H**; Supplementary Fig. S8K–S8N). Together, these findings suggest that mitochondrial K17 stabilizes DHODH by preventing its ubiquitination-mediated degradation.

Lastly, we measured the level of orotate, the product of DHODH, using MS in K17$^+$, K17$^-$, and K17-mMLS L3.6 cells. As expected, we observed a twofold increase in orotate levels in K17$^+$ cells compared with K17$^-$ cells (**Fig. 4I**). Consistent with our finding that mitochondrial K17 stabilizes DHODH, K17-mMLS cells showed lower orotate levels compared with K17$^+$ cells (**Fig. 4J**). Metabolomics profiling further revealed significantly decreased pyrimidine pools in mMLS-K17 cells compared with WT K17$^+$ cells, approaching levels comparable with those in K17$^-$ cells (Supplementary Fig. S8O). Of note, although intracellular CTP was significantly increased in K17$^+$ cells (Supplementary Fig. S8P), both CDP and CTP were decreased in mMLS-K17 cells (Supplementary Fig. S8O), potentially due to lowered mitochondrial DHODH activity. Together, these data suggest that K17 binds to and stabilizes mitochondrial DHODH, thereby enhancing *de novo* pyrimidine biosynthesis that drives resistance to gemcitabine.

Blocking the entry of K17 into the mitochondria or inhibiting DHODH sensitizes K17$^+$ pancreatic cancer cells to gemcitabine

Based on our findings that K17 promotes gemcitabine resistance and interacts with mitochondrial DHODH to upregulate pyrimidine biosynthesis, we postulated that mitochondrial localization of K17 is required to promote resistance to gemcitabine. Consistent with our hypothesis, mMLS-K17 cells were twice as sensitive to gemcitabine but showed increased resistance to brequinar compared with WT K17$^+$ cells (**Fig. 5A** and **B**; Supplementary Fig. S9A and S9B). Furthermore, combination treatment of gemcitabine and brequinar selectively killed WT K17$^+$ but not mMLS-K17 or K17$^-$ cells (**Fig. 5C**; Supplementary Fig. S9C). To validate the dependency of K17$^+$ cells on DHODH to resist gemcitabine, we knocked down DHODH in K17$^+$ and K17$^-$ cells using siRNAs (**Fig. 5D**). The knockdown of DHODH specifically increased the sensitivity to gemcitabine in K17$^+$ cells (around twofold) but not in K17$^-$ cells (**Fig. 5E**). These findings were further validated in mouse PDAC cell lines (**Fig. 5F** and **G**). Notably, exogenous dC abolished sensitivity to brequinar in K17$^+$ cells and conferred even greater resistance in K17$^-$ cells (Supplementary Fig. S9D–S9G). These results indicate that preventing K17 mitochondrial localization or targeting DHODH could be a strategy to overcome gemcitabine resistance in K17$^+$ PDAC cells.

We next tested whether pharmacologic targeting of DHODH sensitizes K17$^+$ PDAC cells, but not K17$^-$ cells, to gemcitabine. We found that cotreatment of brequinar and gemcitabine produced strong synergistic effects in K17$^+$ cells but not in K17$^-$ cells in the

(*Continued*.) ANOVA followed by the Tukey test; #, $P = 0.0665$. **C,** Western blots show immunoprecipitation (IP) of K17 with DHODH and COX IV in cytosolic and mitochondrial fractions from K17 LOF and rescue cell line models. An input control of cell lysates is included. Note: COX IV, K17, and β-actin were intentionally reused in **Fig. 3E**. **D,** DHODH half-life determined by CHX chase assay. α-Tubulin (L3.6, KPC, and L3.6 KO) and β-actin (PANC-1) were used as loading controls. Cyt c, cytochrome c. **E,** Quantification of mitochondrial DHODH degradation over time in L3.6 K17 LOF, KPC and PANC-1 K17 SE, and L3.6 K17 rescue cell line models. Mean ± SD; $n = 3$; two-way ANOVA followed by the Šidák test. **F,** Western blots for ubiquitin in mitochondrial fractions following DHODH immunoprecipitation in K17 LOF, SE, and rescue cell line models. IgG immunoprecipitation controls are included. **G,** Bar graphs show the fold change of DHODH ubiquitination across the isogenic cell line models. Welch *t* test. #, $P = 0.0583$. **H,** DHODH degradation determined by CHX and MG132 assays in K17 LOF, SE, and rescue cell line models. Cells were treated with CHX alone or CHX and MG132 for 8 hours before harvested for Western blots. α-Tubulin (KPC) and β-actin (L3.6, PANC-1, and L3.6 KO) were used as loading controls. **I,** Intracellular orotate levels measured by MS in K17 LOF and SE cell line models. Mean ± SD; $n = 3$ per group; Welch *t* test. **J,** Fold change of intracellular orotate levels in L3.6 KO cells expressing EV, K17, or mMLS. One-way ANOVA followed by the Tukey test. ns, not significant, *, $P < 0.05$; **, $P < 0.01$; ***, $P < 0.001$.

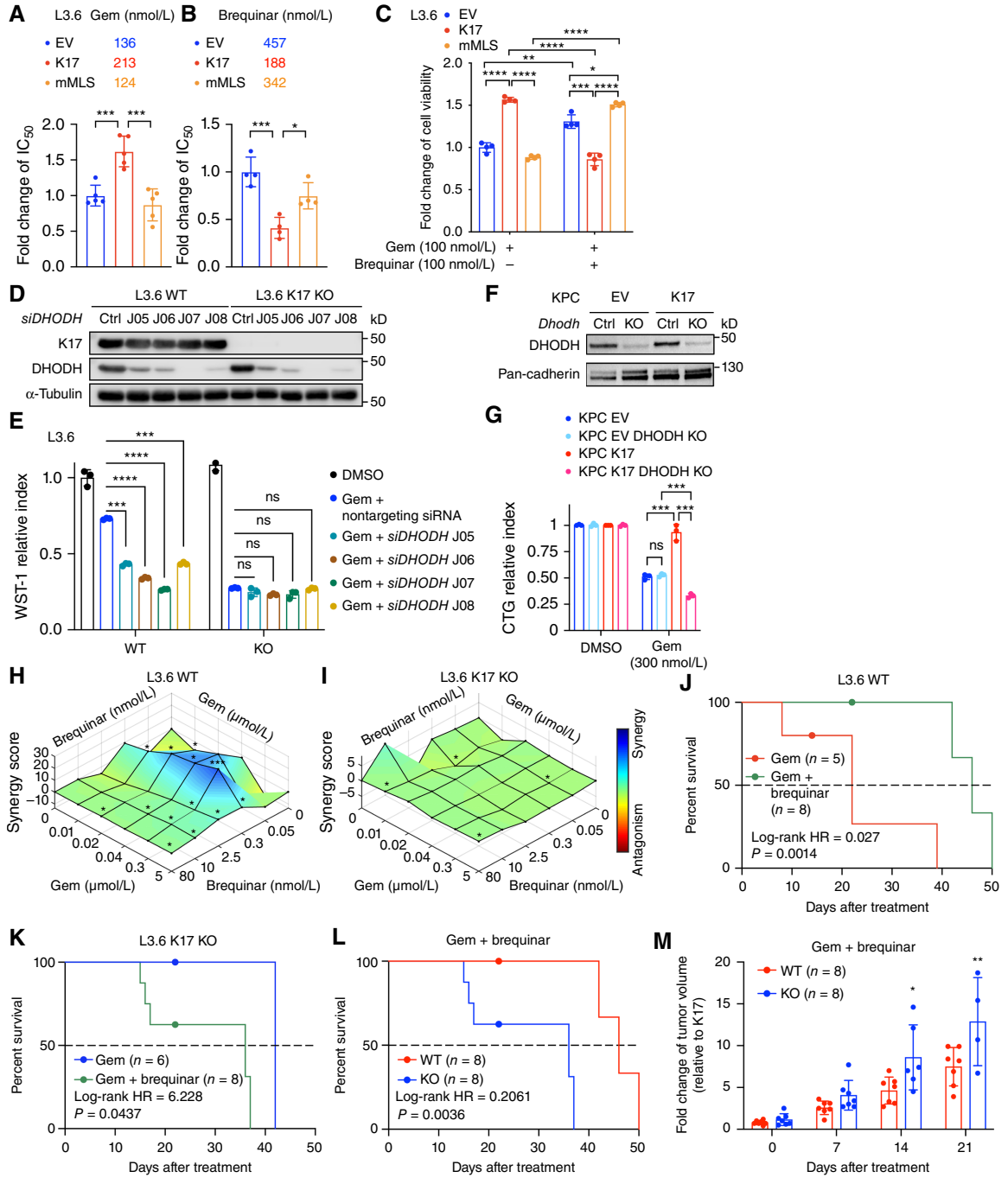

Figure 5.

Brequinar synergizes with gemcitabine to eliminate K17-expressing pancreatic cancer cells. **A** and **B,** IC_{50} values of gemcitabine (Gem; **A**) or brequinar (**B**) in L3.6 (EV, K17, and mMLS-K17) cell line models. Mean ± SD; $n = 5$; one-way ANOVA followed by the Tukey test. **C,** Cell viability following treatment of gemcitabine and brequinar in L3.6 (EV, K17, and mMLS-K17) cell line models. Cells were treated with gemcitabine alone for 48 hours or brequinar for 24 hours followed by gemcitabine for 24 hours. Data are normalized to EV groups. Mean ± SD; $n = 4$; two-way ANOVA followed by the Šídák test. **D,** Western blots show DHODH expression following siRNA-mediated knockdown against DHODH in L3.6 K17 LOF cell line models. **E,** Cell viability of L3.6 K17 LOF cell line models transfected with siRNAs against DHODH or nontargeting siRNA following treatment of gemcitabine. Mean ± SD; $n = 3$; two-way ANOVA followed by the Tukey test. **F,** Western blots show CRISPR–Cas9–mediated DHODH KO in KPC K17 SE cell line models. **G,** Cell viability of KPC K17 SE cell line models following DHODH knockdown and gemcitabine treatment. Mean ± SD; $n = 3$; Welch test. **H** and **I,** Combination treatment of brequinar and gemcitabine in L3.6 K17 LOF cell line models. The synergy distribution is indicated by colors. **J** and **K,** Kaplan–Meier survival curves of mice bearing L3.6 $K17^+$ (**J**) or $K17^-$ (**K**) orthotopically transplanted PDACs following treatment with gemcitabine alone or the combination of brequinar and gemcitabine. (*Continued on the following page.*)

L3.6 K17 LOF and KPC K17 SE cell line models (**Fig. 5H** and **I**; Supplementary Fig S9H). Interestingly, these effects were not detected in the PANC-1 cell line models (Supplementary Fig. S9I), potentially due to phenotypic differences, including high GATA1 expression, that may confer gemcitabine resistance through an alternative mechanism (58). Considering the role of DHODH in the electron transport chain, we performed cotreatment experiments combining gemcitabine with two oxidative phosphorylation inhibitors (FCCP and Gboxin). We observed neutral synergy scores in L3.6 K17 LOF and KPC K17 SE cell line models (Supplementary Fig. S9J and S9K), indicating that targeting oxidative phosphorylation does not synergize with gemcitabine in K17$^+$ pancreatic cancer cells, in contrast to direct DHODH inhibition with brequinar.

Finally, we conducted xenograft studies to validate the synergistic effect of combining gemcitabine and brequinar against K17$^+$ tumors. First, we orthotopically implanted L3.6 K17 WT or K17 KO human pancreatic cancer cells into the head of the pancreas of immunosuppressed mice. Treatments were administered after tumor volume reached 50 mm^3 for long-term survival analyses (**Fig. 5J–M**; Supplementary Fig S10A–S10J). Excitingly, we found the combination treatment of gemcitabine plus brequinar doubled the survival of mice bearing K17 WT tumors in comparison with mice treated with gemcitabine alone (**Fig. 5J**). In contrast, this combination did not offer any survival advantage and may even have shortened survival of mice bearing K17 KO tumors versus mice treated with only gemcitabine (**Fig. 5K**). Supporting these findings (**Fig. 5L** and **M**; Supplementary Fig. S10A–S10D), survival analysis revealed a clear therapeutic advantage of brequinar and gemcitabine in mice bearing K17 WT tumors, with a significantly extended median survival (46 days in WT vs. 36 days in K17 KO, log-rank HR = 0.2061, $P = 0.0036$) and decreased tumor growth. These results suggest that brequinar in combination with gemcitabine synergizes to decrease tumor growth and extend animal survival. Collectively, our study establishes K17 expression as a prerequisite for this metabolic reprogramming (**Fig. 6**), providing a strong rationale to selectively target DHODH in K17$^+$ pancreatic cancer to enhance therapeutic efficacy.

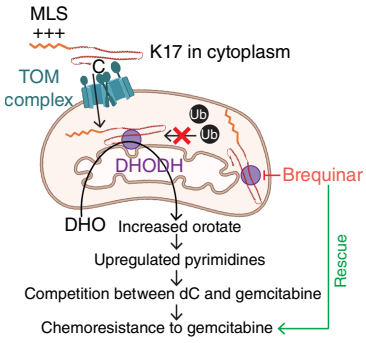

Figure 6.
Summary of key findings. K17 translocates into mitochondria through a functional MLS. Within the mitochondrial intermembrane space, K17 interacts with and stabilizes DHODH by preventing its ubiquitination. K17-mediated stabilization enhances *de novo* pyrimidine biosynthesis, elevates deoxycytidine levels, and drives chemoresistance to gemcitabine. The sensitivity of K17$^+$ cells to brequinar highlights DHODH as a potential therapeutic target in K17-expressing pancreatic cancer. Created in BioRender. Pinto medici, N. (2026) https://BioRender.com/k6ed1uz.

Discussion

Elucidating the mechanisms underlying chemoresistance in basal-like PDAC is critical for developing novel therapeutics and strategies to improve patient survival (59, 60). Resistance to anticancer nucleoside analogues can arise from altered drug transport, metabolic enzyme activity, and the tumor microenvironment (60). For instance, gemcitabine resistance has been linked to reduced nucleoside transporter–mediated uptake (61), enhanced *de novo* dC biosynthesis (62), or increased extracellular dC that competes with drug efficacy (63). Here, we uncover a novel mechanism of mitochondrial localization of K17 and its subsequent stabilization of DHODH. K17 encodes an MLS, enabling its import into mitochondria, in which it localizes to the intermembrane space, binds DHODH, and protects it from degradation. This K17–DHODH axis in the mitochondria promotes *de novo* pyrimidine synthesis and drives gemcitabine resistance. Consistently, we show that increased intracellular dC confers resistance, supporting a molecular competition mechanism and highlighting altered metabolism as a key driver of chemoresistance (62, 63). Although we have not directly investigated K17-driven resistance to 5-FU, another pyrimidine analogue used to treat PDAC (30), we speculate that K17$^+$ cells may employ a similar pyrimidine metabolism–based mechanism to confer resistance to both 5-FU and gemcitabine.

Few studies have investigated the functional role of K17 in cancer metabolism. One report showed that K17 regulates glycolysis via the Akt/mTOR/hypoxia-inducible factor 1α pathway in osteosarcoma, with K17 knockdown suppressing glycolysis *in vitro* (64). In contrast, in pancreatic cancer, our data show that K17-driven glycolytic reprogramming is context and model dependent and less consistent, whereas its impact on *de novo* pyrimidine biosynthesis is more robust and conserved, as demonstrated by steady-state metabolomics and dynamic flux tracing experiments. Our findings thus provide a strong rationale for therapeutically targeting K17-driven *de novo* pyrimidine biosynthesis.

Recent studies have shown that DHODH contributes to chemoresistance in liver cancer (54), and targeting *de novo* pyrimidine biosynthesis synergizes with BCL-xL inhibition to suppress pancreatic cancer (65). Our study demonstrates that both genetic depletion and pharmacologic inhibition of DHODH effectively resensitizes K17$^+$ pancreatic cancer cells to gemcitabine. This selective vulnerability is driven by the increased mitochondrial DHODH content in K17$^+$ cells. Notably, K17$^-$ and mMLS-K17 cancer cells did not benefit from the combination treatment, which we speculate may result from brequinar-induced activation of the nucleoside salvage pathway under predominant DHODH inhibition (66–68), potentially conferring resistance to gemcitabine by mitigating its impact on DNA replication and repair (69). Crucially, the combination of brequinar and gemcitabine achieved a mouse

(*Continued*.) **L,** Kaplan–Meier survival curves of mice bearing L3.6 K17$^+$ or K17$^-$ orthotopically transplanted PDACs following treatment with brequinar and gemcitabine. Log-rank hazard ratios (HR) and *P* values are shown. Dots are censored points. **M,** Fold change in tumor volume over time following combined gemcitabine and brequinar treatment in mice bearing L3.6 K17$^+$ or K17$^-$ orthotopically transplanted PDACs. Mean ± SD; $n = 8$; Welch test. ns, not significant, *, $P < 0.05$; **, $P < 0.01$; ***, $P < 0.001$; ****, $P < 0.0001$.

survival benefit comparable with another effective strategy we previously identified (podophyllotoxin and gemcitabine; ref. 30) in K17$^+$ PDACs, reinforcing its therapeutic potential. These findings provide a new perspective on the historical failure of the DHODH inhibitor brequinar in clinical trials conducted over 3 decades ago; those trials (16, 70, 71), which showed minimal efficacy in unselected patient cohorts, were likely undermined by the lack of a predictive biomarker. Our findings establish K17 as a putative predictive biomarker for identifying patients most likely to benefit from DHODH-targeted therapy.

Our discovery of the mitochondrial K17–DHODH axis reveals a profound metabolic dependency in K17$^+$ basal-like PDACs. This was further substantiated by our analysis of patient data, which demonstrates that upregulation of *de novo* pyrimidine, but not purine, biosynthesis is associated with significantly shorter survival exclusively in patients with high-K17 tumors. Experimentally, K17$^+$ PDAC cells are highly vulnerable to inhibitors of *de novo* pyrimidine synthesis but resistant to inhibitors of both the purine and pyrimidine salvage pathways. This dependency establishes DHODH as a critical metabolic node in K17-driven chemoresistance. Of note, K17-associated therapeutic resistance may reflect cancer cell plasticity, which enables malignant cells in basal-like PDAC to proliferate, differentiate, and adapt to stress (7, 8). Cancer plasticity has also been shown to induce resistance to both chemotherapy and targeted therapy (72). Future studies are warranted to investigate how K17 intersects with cancer metabolism to promote plasticity-driven therapeutic evasion. In conclusion, our study defines a novel connection among K17, mitochondrial function, and nucleotide metabolism, providing a compelling rationale to resurrect DHODH inhibitors in the clinic. By using K17 expression as a predictive biomarker, we can now design targeted trials to overcome gemcitabine resistance and improve therapeutic outcomes for this aggressive malignancy.

Data Availability

TCGA Pan-Cancer Atlas dataset analyzed in this study were obtained from UCSC Xena Browser (https://xenabrowser.net/datapages/?cohort=TCGA%20Pan-Cancer%20(PANCAN)&removeHub=https%3A%2F%2Fxena.treehouse.gi.ucsc.edu%3A443%27). The RNA-seq data generated in this study are publicly available in the Gene Expression Omnibus at GSE323322. All other raw data generated in this study are available upon request to the corresponding author.

Authors' Disclosures

P.K. Singh reports grants from National Cancer Institute (NCI)/NIH during the conduct of the study, as well as grants from NCI/NIH outside the submitted work. K.R. Shroyer reports nonfinancial support and other support from KDX Diagnostics outside the submitted work, as well as a patent for NTD number R-8599 (filed: S/N: 18/051,551) pending, a patent for number 11092603 (filed: October 27, 2016; date of patent: August 17, 2021) issued, and a patent for Keratin 17 as a Biomarker for Bladder Cancer with US patent publication number 2020028479 (filed: August 4, 2017; publication date: September 10, 2020; European patent granted: June 21, 2021), and a patent for application number 17 837 731.3-1111, Ref F009947 issued and licensed to KDX Diagnostics. L.F. Escobar-Hoyos reports other support from KDX Diagnostics during the conduct of the study; grants from NIH R01CA274355-01, NIH DP2CA280625-01, Dr. Ralph and Marian Falk Medical Research Trust, Pershing Square Foundation, Robert L. Fine Cancer Research Foundation, Cancer Research Institute, and The Pew Charitable Trusts outside the submitted work; and a patent for WO2017075174 licensed to KDX Diagnostics, a patent for US2017/045421 licensed to KDX Diagnostics, a patent for WO2016141269A1 licensed to KDX Diagnostics, and a patent for WO2015021346-A1 licensed to OncoGenesis. No disclosures were reported by the other authors.

Authors' Contributions

C.-H. Pan: Conceptualization, data curation, formal analysis, investigation, visualization, methodology, writing–original draft, writing–review and editing. **Y. Lyu:** Conceptualization, data curation, formal analysis, visualization, methodology, writing–review and editing. **M. Ghosh:** Conceptualization, data curation, formal analysis, writing–review and editing. **M.A. Siraj:** Data curation, formal analysis. **R. Tseng:** Data curation, formal analysis. **N.V. Chaika:** Data curation, formal analysis. **J.D. Haley:** Formal analysis, methodology. **B. Khalvatifahlylani:** Data curation. **D.A. Tuveson:** Resources. **H.D. Patel:** Resources, data curation. **M. Faruque:** Resources. **G.H. Rajacharya:** Data curation, formal analysis. **K.L. Donnelly:** Data curation, formal analysis. **C.V. Leiton:** Conceptualization, data curation, formal analysis. **C.M. Mejia Arbelaez:** Data curation, formal analysis. **H. Chen:** Formal analysis. **S. Chowdhury:** Data curation, formal analysis. **S. Sarkar:** Formal analysis. **L. Delgado Coka:** Resources, data curation, formal analysis, writing–review and editing. **L. Roa-Peña:** Data curation. **M. Horowitz:** Data curation. **N. Marchenko:** Conceptualization, supervision, writing–review and editing. **P.K. Singh:** Conceptualization, supervision, methodology. **K.R. Shroyer:** Conceptualization, supervision, funding acquisition, writing–review and editing. **L.F. Escobar-Hoyos:** Conceptualization, supervision, funding acquisition, writing–review and editing.

Acknowledgments

The authors thank all members of Dr. Shroyer's laboratory for their valuable insights, constructive feedback, and continued support throughout this project. The authors also appreciate the expert technical assistance and the collaborative spirit from members of Dr. Escobar-Hoyos laboratory. The authors thank Dr. Coulombe Pierre (University of Michigan) for providing the K17 antibody, Dr. Wei-Xing Zong (Rutgers University) for the L3.6 cells, Dr. Gerardo Mackenzie (University of California at San Diego) for the KPC cells, the Yale Center for Molecular Discovery, and the Stony Brook University Proteomics Center for performing key experiments. ChatGPT was used to improve language quality and clarity. C-H Pan is supported by PF-25-1422234-01-PFCBI from the American Cancer Society, ACS Fairfield County CT Research Council, https://doi.org/10.53354/ACS.PF-25-1422234-01-PFCBI.pc.gr.230344. This study was funded by the NCI/NIH (K99-R00CA226342, R01CA274355, and DP2CA280625), the Dr. Ralph and Marian Falk Medical Research Trust, Bank of America, the Damon Runyon Cancer Research Foundation, the AACR Career Development Award for Pancreatic Cancer Research, the Pershing Square Sohn Cancer Prize, The Robert L. Fine Cancer Research Foundation, the Pew-Stewart Scholars for Cancer Research, and the Mary Louise Lopez Fund for Pancreatic Cancer Research (to LF Escobar-Hoyos). This work was also supported by Academic Enrichment Funds of the Department of Pathology at the Renaissance School of Medicine, the Marvin Kuschner endowed professorship of Stony Brook University, and the Pancreatic Cancer Action Network Translational Research Grant 18-65-SHRO (to KR Shroyer).

Note

Supplementary data for this article are available at Cancer Research Online (http://cancerres.aacrjournals.org/).

Received October 6, 2025; revised January 26, 2026; accepted March 6, 2026; posted first March 12, 2026.

References

1. Moffitt RA, Marayati R, Flate EL, Volmar KE, Loeza SG, Hoadley KA, et al. Virtual microdissection identifies distinct tumor- and stroma-specific subtypes of pancreatic ductal adenocarcinoma. Nat Genet 2015;47:1168–78.
2. Bailey P, Chang DK, Nones K, Johns AL, Patch AM, Gingras MC, et al. Genomic analyses identify molecular subtypes of pancreatic cancer. Nature 2016;531:47–52.
3. Collisson EA, Bailey P, Chang DK, Biankin AV. Molecular subtypes of pancreatic cancer. Nat Rev Gastroenterol Hepatol 2019;16:207–20.
4. Aung KL, Fischer SE, Denroche RE, Jang GH, Dodd A, Creighton S, et al. Genomics-driven precision medicine for advanced pancreatic cancer: early results from the COMPASS trial. Clin Cancer Res 2018;24:1344–54.
5. Zhou X, An J, Kurilov R, Brors B, Hu K, Peccerella T, et al. Persister cell phenotypes contribute to poor patient outcomes after neoadjuvant chemotherapy in PDAC. Nat Cancer 2023;4:1362–81.

6. Williams HL, Dias Costa A, Zhang J, Raghavan S, Winter PS, Kapner KS, et al. Spatially resolved single-cell assessment of pancreatic cancer expression subtypes reveals co-expressor phenotypes and extensive intratumoral heterogeneity. Cancer Res 2023;83:441–55.
7. Pitter KL, Grbovic-Huezo O, Joost S, Singhal A, Blum M, Wu K, et al. Systematic comparison of pancreatic ductal adenocarcinoma models identifies a conserved highly plastic basal cell state. Cancer Res 2022;82:3549–60.
8. Singhal A, Styers HC, Rub J, Li Z, Torborg SR, Kim JY, et al. A classical epithelial state drives acute resistance to KRAS inhibition in pancreatic cancer. Cancer Discov 2024;14:2122–34.
9. Delgado-Coka LA, Roa-Peña L, Babu S, Horowitz M, Petricoin EF 3rd, Matrisian LM, et al. Keratin 17 is a prognostic and predictive biomarker in pancreatic ductal adenocarcinoma. Am J Clin Pathol 2024;162:314–26.
10. Alvarellos ML, Lamba J, Sangkuhl K, Thorn CF, Wang L, Klein DJ, et al. PharmGKB summary: gemcitabine pathway. Pharmacogenet Genomics 2014;24:564–74.
11. Braun LM, Lagies S, Guenzle J, Fichtner-Feigl S, Wittel UA, Kammerer B. Metabolic adaptation during nab-paclitaxel resistance in pancreatic cancer cell lines. Cells 2020;9:1251.
12. Brown KK, Spinelli JB, Asara JM, Toker A. Adaptive reprogramming of de novo pyrimidine synthesis is a metabolic vulnerability in triple-negative breast cancer. Cancer Discov 2017;7:391–9.
13. Zhao S, Francois A, Kidane D. Inhibition of DHODH enhances replication-associated genomic instability and promotes sensitivity in Endometrial Cancer. Cancers (Basel) 2023;15:5727.
14. Alfaro-Lara R, Espinosa-Ortega HF, Arce-Salinas CA; PRECIS study group, all physicians belong to Division of Internal Medicine. Hospital Central Sur de Pemex. Systematic review and meta-analysis of the efficacy and safety of leflunomide and methotrexate in the treatment of rheumatoid arthritis. Reumatol Clin (Engl Ed) 2019;15:133–9.
15. Fragoso YD, Brooks JB. Leflunomide and teriflunomide: altering the metabolism of pyrimidines for the treatment of autoimmune diseases. Expert Rev Clin Pharmacol 2015;8:315–20.
16. Moore M, Maroun J, Robert F, Natale R, Neidhart J, Dallaire B, et al. Multicenter phase II study of brequinar sodium in patients with advanced gastrointestinal cancer. Invest New Drugs 1993;11:61–5.
17. Roa-Peña L, Babu S, Leiton CV, Wu M, Taboada S, Akalin A, et al. Keratin 17 testing in pancreatic cancer needle aspiration biopsies predicts survival. Cancer Cytopathol 2021;129:865–73.
18. Roa-Peña L, Leiton CV, Babu S, Pan CH, Vanner EA, Akalin A, et al. Keratin 17 identifies the most lethal molecular subtype of pancreatic cancer. Sci Rep 2019;9:11239.
19. Ide M, Kato T, Ogata K, Mochiki E, Kuwano H, Oyama T. Keratin 17 expression correlates with tumor progression and poor prognosis in gastric adenocarcinoma. Ann Surg Oncol 2012;19:3506–14.
20. Wang YF, Lang HY, Yuan J, Wang J, Wang R, Zhang XH, et al. Overexpression of keratin 17 is associated with poor prognosis in epithelial ovarian cancer. Tumour Biol 2013;34:1685–9.
21. Escobar-Hoyos LF, Shah R, Roa-Peña L, Vanner EA, Najafian N, Banach A, et al. Keratin-17 promotes p27KIP1 nuclear export and degradation and offers potential prognostic utility. Cancer Res 2015;75:3650–62.
22. Kim HS, Lee JJ, Do SI, Kim K, Do IG, Kim DH, et al. Overexpression of cytokeratin 17 is associated with the development of papillary thyroid carcinoma and the presence of lymph node metastasis. Int J Clin Exp Pathol 2015;8:5695–701.
23. Yagyuu T, Obayashi C, Ueyama Y, Takano M, Tanaka Y, Kawaguchi M, et al. Multivariate analyses of Ki-67, cytokeratin 13 and cytokeratin 17 in diagnosis and prognosis of oral precancerous lesions. J Oral Pathol Med 2015;44:523–31.
24. Kim K, Lee HW, Chae SW, Kim DH, Do IG, Lee HJ, et al. Cytokeratin 17 expression is associated with poor prognosis in gallbladder adenocarcinoma. Appl Immunohistochem Mol Morphol 2017;25:346–50.
25. Merkin RD, Vanner EA, Romeiser JL, Shroyer ALW, Escobar-Hoyos LF, Li J, et al. Keratin 17 is overexpressed and predicts poor survival in estrogen receptor-negative/human epidermal growth factor receptor-2-negative breast cancer. Hum Pathol 2017;62:23–32.
26. Shroyer KR, Escobar-Hoyos LF. Keratin 17 as a prognostic marker for pancreatic cancer. United States patent US11092603B2. 2021 Aug 17.
27. Cecchini M, Salem RR, Robert M, Czerniak S, Blaha O, Zelterman D, et al. Perioperative modified FOLFIRINOX for resectable pancreatic cancer: a nonrandomized controlled trial. JAMA Oncol 2024;10:1027–35.
28. Baraks G, Tseng R, Pan CH, Kasliwal S, Leiton CV, Shroyer KR, et al. Dissecting the oncogenic roles of keratin 17 in the hallmarks of cancer. Cancer Res 2022;82:1159–66.
29. Jacob JT, Nair RR, Poll BG, Pineda CM, Hobbs RP, Matunis MJ, et al. Keratin 17 regulates nuclear morphology and chromatin organization. J Cell Sci 2020;133:jcs254094.
30. Pan CH, Otsuka Y, Sridharan B, Woo M, Leiton CV, Babu S, et al. An unbiased high-throughput drug screen reveals a potential therapeutic vulnerability in the most lethal molecular subtype of pancreatic cancer. Mol Oncol 2020;14:1800–16.
31. Nawy T. A pan-cancer atlas. Nat Methods 2018;15:407.
32. Barbie DA, Tamayo P, Boehm JS, Kim SY, Moody SE, Dunn IF, et al. Systematic RNA interference reveals that oncogenic KRAS-driven cancers require TBK1. Nature 2009;462:108–12.
33. Bruns CJ, Harbison MT, Kuniyasu H, Eue I, Fidler IJ. In vivo selection and characterization of metastatic variants from human pancreatic adenocarcinoma by using orthotopic implantation in nude mice. Neoplasia 1999;1:50–62.
34. Tiriac H, Belleau P, Engle DD, Plenker D, Deschenes A, Somerville TDD, et al. Organoid profiling identifies common responders to chemotherapy in pancreatic cancer. Cancer Discov 2018;8:1112–29.
35. Gunda V, Yu F, Singh PK. Validation of metabolic alterations in microscale cell culture lysates using hydrophilic interaction liquid chromatography (HILIC)-tandem mass spectrometry-based metabolomics. PLoS One 2016;11:e0154416.
36. Yuan M, Breitkopf SB, Yang X, Asara JM. A positive/negative ion-switching, targeted mass spectrometry-based metabolomics platform for bodily fluids, cells, and fresh and fixed tissue. Nat Protoc 2012;7:872–81.
37. Xia J, Wishart DS. Using MetaboAnalyst 3.0 for comprehensive metabolomics data analysis. Curr Protoc Bioinformatics 2016;55():14.10.1–91.
38. Zhou D, Zhong S, Han X, Liu D, Fang H, Wang Y. Protocol for mitochondrial isolation and sub-cellular localization assay for mitochondrial proteins. STAR Protoc 2023;4:102088.
39. Zhang S, Reljić B, Liang C, Kerouanton B, Francisco JC, Peh JH, et al. Mitochondrial peptide BRAWNIN is essential for vertebrate respiratory complex III assembly. Nat Commun 2020;11:1312.
40. Di Veroli GY, Fornari C, Wang D, Mollard S, Bramhall JL, Richards FM, et al. Combenefit: an interactive platform for the analysis and visualization of drug combinations. Bioinformatics 2016;32:2866–8.
41. Mathews CK. Deoxyribonucleotide metabolism, mutagenesis and cancer. Nat Rev Cancer 2015;15:528–39.
42. Okesli A, Khosla C, Bassik MC. Human pyrimidine nucleotide biosynthesis as a target for antiviral chemotherapy. Curr Opin Biotechnol 2017;48:127–34.
43. Zhou Y, Tao L, Zhou X, Zuo Z, Gong J, Liu X, et al. DHODH and cancer: promising prospects to be explored. Cancer Metab 2021;9:22.
44. Banerjee R, Purhonen J, Kallijärvi J. The mitochondrial coenzyme Q junction and complex III: biochemistry and pathophysiology. FEBS J 2022;289:6936–58.
45. Löffler M, Fairbanks L, Zameitat E, Marinaki A, Simmonds H. Pyrimidine pathways in health and disease. Trends Mol Med 2005;11:430–7.
46. von Heijne G. Mitochondrial targeting sequences may form amphiphilic helices. EMBO J 1986;5:1335–42.
47. Pfanner N, Warscheid B, Wiedemann N. Mitochondrial proteins: from biogenesis to functional networks. Nat Rev Mol Cell Biol 2019;20:267–84.
48. Sayyed UMH, Mahalakshmi R. Mitochondrial protein translocation machinery: from TOM structural biogenesis to functional regulation. J Biol Chem 2022;298:101870.
49. Neupert W, Herrmann JM. Translocation of proteins into mitochondria. Annu Rev Biochem 2007;76:723–49.
50. Claros MG, Vincens P. Computational method to predict mitochondrially imported proteins and their targeting sequences. Eur J Biochem 1996;241:779–86.
51. Yamamoto H, Itoh N, Kawano S, Yatsukawa Y, Momose T, Makio T, et al. Dual role of the receptor Tom20 in specificity and efficiency of protein import into mitochondria. Proc Natl Acad Sci U S A 2011;108:91–6.
52. Gomes F, Turano H, Ramos A, Netto LES. Assessment of submitochondrial protein localization in budding yeast Saccharomyces cerevisiae. J Vis Exp 2021. 10.3791/62853-v.
53. Rawls J, Knecht W, Diekert K, Lill R, Löffler M. Requirements for the mitochondrial import and localization of dihydroorotate dehydrogenase. Eur J Biochem 2000;267:2079–87.

54. Zhan M, Ding Y, Huang S, Liu Y, Xiao J, Yu H, et al. Lysyl oxidase-like 3 restrains mitochondrial ferroptosis to promote liver cancer chemoresistance by stabilizing dihydroorotate dehydrogenase. Nat Commun 2023;14:3123.
55. Zhang Y, Karmon O, Das K, Wiener R, Lehming N, Pines O. Ubiquitination occurs in the mitochondrial matrix by eclipsed targeted components of the ubiquitination machinery. Cells 2022;11:4109.
56. Lavie J, De Belvalet H, Sonon S, Ion AM, Dumon E, Melser S, et al. Ubiquitin-dependent degradation of mitochondrial proteins regulates energy metabolism. Cell Rep 2018;23:2852–63.
57. Ravanelli S, den Brave F, Hoppe T. Mitochondrial quality control governed by ubiquitin. Front Cel Dev Biol 2020;8:270.
58. Chang Z, Zhang Y, Liu J, Guan C, Gu X, Yang Z, et al. GATA1 promotes gemcitabine resistance in pancreatic cancer through antiapoptotic pathway. J Oncol 2019;2019:9474273.
59. Chand S, O'Hayer K, Blanco FF, Winter JM, Brody JR. The landscape of pancreatic cancer therapeutic resistance mechanisms. Int J Biol Sci 2016;12:273–82.
60. Zeng S, Pöttler M, Lan B, Grützmann R, Pilarsky C, Yang H. Chemoresistance in pancreatic cancer. Int J Mol Sci 2019;20:4504.
61. Rauchwerger DR, Firby PS, Hedley DW, Moore MJ. Equilibrative-sensitive nucleoside transporter and its role in gemcitabine sensitivity. Cancer Res 2000;60:6075–9.
62. Shukla SK, Purohit V, Mehla K, Gunda V, Chaika NV, Vernucci E, et al. MUC1 and HIF-1alpha signaling crosstalk induces anabolic glucose metabolism to impart gemcitabine resistance to pancreatic cancer. Cancer Cell 2017;32:71–87.e7.
63. Halbrook CJ, Pontious C, Kovalenko I, Lapienyte L, Dreyer S, Lee HJ, et al. Macrophage-released pyrimidines inhibit gemcitabine therapy in pancreatic cancer. Cell Metab 2019;29:1390–9.e6.
64. Yan X, Yang C, Hu W, Chen T, Wang Q, Pan F, et al. Knockdown of KRT17 decreases osteosarcoma cell proliferation and the warburg effect via the AKT/mTOR/HIF1alpha pathway. Oncol Rep 2020;44:103–14.
65. Zhang H, Santana-Codina N, Yu Q, Poupault C, Campos C, Qin X, et al. De novo pyrimidine biosynthesis inhibition synergizes with BCL-X(L) targeting in pancreatic cancer. Nat Commun 2025;16:6987.
66. Cuthbertson CR, Guo H, Kyani A, Madak JT, Arabzada Z, Neamati N. The dihydroorotate dehydrogenase inhibitor brequinar is synergistic with ENT1/2 inhibitors. ACS Pharmacol Transl Sci 2020;3:1242–52.
67. Alkasalias T, Zhang J, Madapura H, Dalarun B, Reina OB, Lewensohn R, et al. Proof-of-principle studies on a strategy to enhance nucleotide imbalance specifically in cancer cells. Cell Death Discov 2022;8:464.
68. Li L, Ng SR, Colón CI, Drapkin BJ, Hsu PP, Li Z, et al. Identification of DHODH as a therapeutic target in small cell lung cancer. Sci Transl Med 2019;11:eaaw7852.
69. Mullen NJ, Singh PK. Nucleotide metabolism: a pan-cancer metabolic dependency. Nat Rev Cancer 2023;23:275–94.
70. Dodion PF, Wagener T, Stoter G, Drozd A, Lev LM, Skovsgaard T, et al. Phase II trial with Brequinar (DUP-785, NSC 368390) in patients with metastatic colorectal cancer: a study of the early clinical trials group of the EORTC. Ann Oncol 1990;1:79–80.
71. Maroun J, Ruckdeschel J, Natale R, Morgan R, Dallaire B, Sisk R, et al. Multicenter phase II study of brequinar sodium in patients with advanced lung cancer. Cancer Chemother Pharmacol 1993;32:64–6.
72. Chan JE, Pan CH, Rub J, Guzman G, Krause K, Brown E, et al. Critical role for a high-plasticity cell state in lung cancer. Nature 2026;651:231–41.